The Astrophysical Journal, 1002:194 (19pp), 2026 May 10 https://doi.org/10.3847/1538-4357/ae522d

A Search for Successful and Choked Jets in Nearby Broad-lined Type Ic Supernovae

Tanner O'Dwyer[1], Alessandra Corsi[1], Sheng Yang[2], Shreya Anand[3,20], S. Bradley Cenko[4,5], Gokul P. Srinivasaragavan[6], Anna Y. Q. Ho[7], Jesper Sollerman[8], Bei Zhou[9,10], Arvind Balasubramanian[11], Po-Wen Chang[12], Marc Kamionkowski[1], Daniel Perley[13], Russ R. Laher[14], Kohta Murase[15,16], Frank J. Masci[14], Mansi M. Kasliwal[17], Josiah N. Purdum[18], and Matthew J. Graham[19]

[1] William H. Miller III Department of Physics and Astronomy, Johns Hopkins University, Baltimore, MD 21210-21218, USA
[2] Institute for Gravitational Wave Astronomy, Henan Academy of Sciences, Zhengzhou, Henan 450046, People's Republic of China
[3] Kavli Institute for Particle Astrophysics and Cosmology, Stanford University, 452 Lomita Mall, Stanford, CA 94305, USA
[4] Astrophysics Science Division, NASA Goddard Space Flight Center, 8800 Greenbelt Road, Greenbelt, MD 20771, USA
[5] Joint Space-Science Institute, University of Maryland, College Park, MD 20742, USA
[6] University of Maryland, College Park, MD 20742, USA
[7] Department of Astronomy, Cornell University, Ithaca, NY 14853, USA
[8] Department of Astronomy, Oskar Klein Centre, Stockholm University, SE-10691 Stockholm, Sweden
[9] Theory Division, Fermi National Accelerator Laboratory, Batavia, IL 60510, USA
[10] Kavli Institute for Cosmological Physics, University of Chicago, Chicago, IL 60637, USA
[11] Indian Institute of Astrophysics, Koramangala II Block, Bangalore 560034, India
[12] Lawrence Berkeley National Laboratory, Berkeley, CA 94720, USA
[13] Astrophysics Research Institute, Liverpool John Moores University, 146 Brownlow Hill, Liverpool, L3 5RF, UK
[14] IPAC, California Institute of Technology, 1200 E. California Boulevard, Pasadena, CA 91125, USA
[15] Department of Physics, Department of Astronomy & Astrophysics, Center for Multimessenger Astrophysics, Institute for Gravitationand the Cosmos, The Pennsylvania State University, University Park, PA 16802, USA
[16] Center for Gravitational Physics and Quantum Information, Yukawa Institute for Theoretical Physics, Kyoto University, Kyoto 606-8502, Japan
[17] Division of Physics, Mathematics, and Astronomy, California Institute of Technology, Pasadena, CA 91125, USA
[18] Caltech Optical Observatories, California Institute of Technology, Pasadena, CA 91125, USA
[19] California Institute of Technology, Pasadena, CA 91125, USA
Received 2025 December 9; revised 2026 March 4; accepted 2026 March 14; published 2026 May 6

Abstract

The observational link between long gamma-ray bursts (GRBs) and broad-lined stripped-envelope core-collapse supernovae (SNe Ic-BL) is well established. Significant progress has been made in constraining what fraction of SNe Ic-BL may power high- or low-luminosity GRBs when viewed at small off-axis angles. However, the GRB–SN connection still lacks a complete understanding in the broader context of massive-star evolution and explosion physics. Models predict a continuum of outcomes for the fastest ejecta, from choked to ultrarelativistic jets, and observations from radio to X-rays are key to probing these scenarios across a range of viewing angles and velocities. Here, we present results from a coordinated radio-to-X-ray campaign targeting nearby ($z \lesssim 0.1$) SNe Ic-BL designed to explore this diversity. With eight new radio-monitored events and updated data for one previously observed SN, we further tighten constraints on the fraction of SNe Ic-BL as relativistic as SN 1998bw (GRB 980425). We identify SN 2024rjw as a new radio-loud event likely powered by strong interaction with circumstellar material, and add evidence supporting a similar interpretation for SN 2020jqm. We also establish new limits on the properties of radio-emitting ejecta with velocities consistent with cocoons from choked jets, highlighting SN 2022xxf as a promising cocoon-dominated candidate. These results refine our understanding of the continuum linking ordinary SNe Ic-BL, engine-driven explosions, and GRBs, and contribute to building a sample that will inform future multimessenger searches for electromagnetic counterparts to high-energy neutrinos.

Unified Astronomy Thesaurus concepts: Supernovae (1668); Gamma-ray bursts (629); Radio continuum emission (1340)

1. Introduction

Stripped-envelope core-collapse supernovae (SNe) of Type Ic (hydrogen- and helium-poor) with broad lines (BL) constitute ≈5% of SNe associated with the deaths of massive stars (D. A. Perley et al. 2020). SNe Ic-BL are also the only type of SNe securely associated with gamma-ray bursts (GRBs). The broad lines that characterize SNe Ic-BL optical spectra point to photospheric velocities systematically higher than those measured in ordinary SNe Ic at similar epochs (M. Modjaz et al. 2016; G. P. Srinivasaragavan et al. 2024). The kinetic energies from modeling of optical data of SNe Ic-BL have been inferred to be in the range (4–7) × 10^{51} erg on average, in excess of the ≈10^{51} erg inferred in typical SNe Ibc (F. Taddia et al. 2019; Ó. Rodríguez et al. 2023; G. P. Srinivasaragavan et al. 2024).

The jet-engine model is a compelling scenario invoked to explain the velocities and energies of SNe Ic-BL (e.g., D. Lazzati et al. 2012; E. Nakar & T. Piran 2017; F. De Colle et al. 2022; M. Eisenberg et al. 2022; M. Pais et al. 2023). In this scenario, successful relativistic jets powering long GRBs are rare outcomes of massive core collapses, and are observed in only ∼1% of all SNe Ibc (A. M. Soderberg et al. 2010). However, jet engines could still play a role in SNe Ic-BL and

[20] LSST-DA Catalyst Fellow.

low-luminosity GRBs. Low-luminosity gamma-ray bursts (or LLGRBs) are a class of GRBs characterized by a lower isotropic-equivalent energy range (10^{46}–10^{48}erg s^{-1}) than other classes of GRBs (E. Liang et al. 2007; E. Nakar 2015; Z. Cano et al. 2017). In fact, a more common outcome of the jet-engine model is that of a choked jet—one that is unable to break out of the surrounding dense matter from the stellar atmosphere that the jet has to cross to produce the bright gamma rays observed in a long GRB. Even though a choked jet does not emerge, a cocoon forms as the jet drives its way through the stellar envelope, spilling hot material sideways. This cocoon may produce observable signatures (D. Lazzati et al. 2012; E. Nakar & T. Piran 2017; F. De Colle et al. 2018, 2022). Specifically, the breakout of the cocoon can produce a bright flash sufficiently powerful to explain the origin of low-luminosity GRBs, such as the famous GRB 980425, associated with the SN Ic-BL 1998bw (S. R. Kulkarni et al. 1998; F. Patat et al. 2001; E. Nakar & R. Sari 2012). Nonthermal synchrotron radiation produced in the cocoon shock front can also explain the radio emission observed in relativistic SNe without a GRB counterpart (F. De Colle et al. 2018), such as SN 2009bb (A. M. Soderberg et al. 2010).

A key question that remains open in the jet-engine scenario is whether SNe Ic-BL that are not associated with GRBs harbor jet engines. If they do, then their jets could be choked, or successful but largely off-axis.

SNe Ic-BL are now being discovered (and their discoveries promptly announced publicly) by large time-domain surveys of the sky at a much increased rate, enabling systematic follow-up observations. Observations of the closest SNe Ic-BL with the Karl G. Jansky Very Large Array (VLA; R. A. Perley et al. 2011), presented in A. Corsi et al. (2023) and G. P. Srinivasaragavan et al. (2024), have established two key facts. First, SNe Ic-BL (as opposed to any SN Ibc) producing 1998bw-like (i.e., low-luminosity GRB) jets are rare (<19%; A. Corsi et al. 2023), though they still may be more common than those producing long GRBs (≈1%–5% of the SNe Ibc; A. M. Soderberg et al. 2006b). Second, the population of SNe Ic-BL with radio detections and radio nondetections are indistinct from one another with respect to their optically inferred explosion properties, and there are no statistically significant correlations present between the events' radio luminosities and optically inferred explosion properties (G. P. Srinivasaragavan et al. 2024). Hence, optical data alone cannot provide inferences on the radio properties of SNe Ic-BL as related to their fastest ejecta, underscoring the importance of radio observations.

In this paper, we further tighten the limits on the rate of SNe Ic-BL as relativistic as SN 1998bw (GRB 980425), expanding upon the results of A. Corsi et al. (2023), and we establish new constraints on the properties of radio-emitting ejecta with velocities consistent with cocoons potentially produced by choked jets. Besides their importance for understanding the physics of massive-star explosions, choked jets are interesting in the context of multimessenger astronomy (e.g., A. Corsi et al. 2024; A. Zegarelli et al. 2024, and references therein), as theoretical models suggest that they may lead to high-energy (HE) neutrino emission while the coproduced gamma rays are absorbed (e.g., N. Senno et al. 2016). In fact, several searches of HE neutrino detector data have targeted both GRBs (e.g., M. G. Aartsen et al. 2015, 2016; R. Abbasi et al. 2022) and potential choked-jet emission associated with core-collapse SNe (e.g., R. Abbasi et al. 2012, 2023; P.-W. Chang et al. 2024); however, so far, these searches have not specifically targeted large samples of SNe Ic-BL showing evidence for fast ejecta components in the radio. Our work contributes to building such a sample.

Our paper is organized as follows. In Section 2, we present the multiwavelength observations of the SNe in our sample. In Section 3, we discuss our analysis of the collected multiwavelength data. In Section 4, we discuss the multimessenger prospects, highlighting HE neutrino contributions. In Section 5, we summarize our results and present our conclusions.

2. Multiwavelength Observations

We have collected a sample of nine SNe, eight classified as Type Ic-BL and one as Type Ic, observed with the Zwicky Transient Facility (ZTF; E. C. Bellm et al. 2019; M. J. Graham et al. 2019; F. J. Masci et al. 2019; S. J. van der Walt et al. 2019; R. Dekany et al. 2020; M. W. Coughlin et al. 2023) and with follow-up observations in the radio (Table 1). Of these SNe, eight were not included in previous radio studies of SNe Ic-BL with deep VLA observations (A. Corsi et al. 2023, 2016). Two of the SNe (SN 2020jqm and SN 2021ywf) were included in A. Corsi et al. (2023), but here we present additional radio follow-up observations. SN 2024rjw was initially classified as a Type Ic-BL SN by C. Angus (2024), but later recognized to be a regular SN Ic. We include this source in our sample as it serves as a comparison for nearby stripped-envelope core-collapse SNe that are not expected to host jet engines.

The SNe included in our sample were selected among those monitored through the ZTF Bright Transient Survey (C. Fremling et al. 2020; D. A. Perley et al. 2020) based on their spectral classification as Type Ic-BL and the availability of VLA observing time. The last was predominantly obtained through joint observing programs of the Neil Gehrels Swift Observatory (N. Gehrels et al. 2004) and the VLA, targeting SNe Ic-BL located at $d_L \lesssim 150$ Mpc (this distance enables the probing of relativistic ejecta with relatively short VLA observations). Given these selection criteria, the median redshift of the SNe in our sample ($z \approx 0.026$) is smaller than that of SNe Ic-BL considered in previous studies, such as A. Corsi et al. (2023; average redshift $z_{\rm avg} \approx 0.037$), F. Taddia et al. (2019; average redshift $z_{\rm avg} \approx 0.076$), and of the larger ZTF SN Ic-BL sample presented in G. P. Srinivasaragavan et al. (2024; average redshift $z_{\rm avg} \approx 0.042$).

We note that the ZTF has contributed to most of the SN detections considered here. Two of the SNe in our sample (SN 2022crr and SN 2024abup) were discovered by the Asteroid Terrestrial-impact Last Alert System (ATLAS; J. L. Tonry et al. 2018). SN 2023eiw was first reported by the Panoramic Survey Telescope and Rapid Response System (Pan-STARRS1; K. C. Chambers et al. 2016). In what follows, we describe the observations carried out for this work. In Section 5, we give more details on each of the SNe Ic-BL in our sample.

2.1. ZTF Photometry

Photometric observations were obtained with the Palomar Schmidt 48-inch (P48) Samuel Oschin telescope as part of the ZTF survey (E. C. Bellm et al. 2019; M. J. Graham et al. 2019), using the ZTF camera (R. Dekany et al. 2020). In default observing mode, ZTF uses 30 s exposures, with survey observations carried out in the r and g bands, down to a typical

Table 1
The Sample of Nine SNe Analyzed in This Work

SN	ZTF Name	T_0 (MJD)	R.A./Decl. (J2000) (hh:mm:ss dd:mm:ss)	z	d_L (Mpc)	Type
2020jqm	ZTF20aazkjfv	58980.27	13:49:18.56 −03:46:10.27	0.037	164	Ic-BL
2022xzc	ZTF22abnpsou	59869.53	12:01:12.59 +22:36:55.23	0.027	119	Ic-BL
2022crr	ZTF22aabgazg	59628.50	15:24:49.13 −21:23:21.73	0.019	82.2	Ic-BL
2022xxf	ZTF22abnvurz	59870.53	11:30:05.94 +09:16:57.37	0.003	13.0	Ic-BL
2023eiw	ZTF19aawhzsh	60033.40	12:28:46.20 +46:31:15.64	0.025	110	Ic-BL
2023zeu	ZTF18abqtnbk	60287.11	01:36:49.25 +01:35:05.68	0.03	132	Ic-BL
2024abup	ZTF24abvtbyt	60636.35	01:49:11.32 −10:25:27.44	0.0058	25.1	Ic-BL
2024adml	ZTF24abwsaxu	60650.46	10:10:40.48 −02:26:05.14	0.037	164	Ic-BL
2024rjw	ZTF24aayimjt	60525.30	21:03:10.11 +20:45:02.58	0.02	87.5	Ic

Note. For each SN we list, from left to right, the IAU name; the ZTF name; the MJD of discovery (T_0); the sky position (R.A. and decl.); the redshift (z); the luminosity distance (d_L); and the spectral type.

limiting magnitude of ≈20.5 mag. We queried the photometric data from the ZTF forced-photometry service (F. J. Masci et al. 2019). For SN 2023eiw and SN 2024abup, the ZTF observations were sparse, so we used forced-photometry data from ATLAS (J. L. Tonry et al. 2018).

We corrected all ZTF and ATLAS photometry for Galactic extinction using $E(B-V)$ values toward the SN positions derived from E. F. Schlafly & D. P. Finkbeiner (2011). All reddening corrections were applied using the J. A. Cardelli et al. (1989) extinction law with $R_V = 3.1$. The light curves of all the SNe in our sample are shown in Figure 1. We discuss the optical light-curve analysis in Section 3 and summarize the results of this analysis in Table 2. All the light curves and spectra presented in this work will be made public via Weizmann Interactive Supernova Data Repository[21] (or WISeREP; O. Yaron & A. Gal-Yam 2012).

2.2. Optical Spectroscopy

Preliminary classifications of the SNe in our sample were obtained with either the Spectral Energy Distribution Machine (SEDM; N. Blagorodnova et al. 2018; M. Rigault et al. 2019; Y.-L. Kim et al. 2022) or the Double Spectrograph (DBSP; J. B. Oke et al. 1995). The SEDM is a low-resolution ($R \sim 100$) integral field unit spectrograph optimized for transient classification with high observing efficiency, mounted on the Palomar 60-inch telescope (P60; S. B. Cenko et al. 2006). The DBSP is a low- to medium-resolution grating spectrograph, mounted at the Cassegrain focus of the Palomar 200-inch Hale Telescope (J. B. Oke & J. E. Gunn 1982).

After initial classification, further spectroscopic observations are typically carried out as part of the ZTF transient programs to confirm and/or improve the classification, and to characterize the evolving spectral properties of interesting events. From the series of spectra obtained for each SN, we select one high-quality photospheric-phase spectrum (shown in gray in Figure 2). We analyze this with `Astrodash` (D. Muthukrishna et al. 2019) to obtain the best match to a SN Ic-BL template (black) after clipping the host emission lines and fixing the redshift to that derived either from the Sloan Digital Sky Survey (SDSS) host-galaxy spectrum or from spectral line fitting (Hα; see the appendices for further details). In addition to SEDM and DBSP, we also utilized the Low Resolution Imaging Spectrometer (LRIS; J. B. Oke & J. E. Gunn 1982; J. B. Oke et al. 1995), a visible-wavelength imaging and spectroscopy instrument operating at the Cassegrain focus of Keck I (J. B. Oke et al. 1995), and the Alhambra Faint Object Spectrograph and Camera (ALFOSC), a CCD camera and spectrograph installed at the Nordic Optical Telescope (NOT; A. A. Djupvik & J. Andersen 2010).

2.3. X-Ray Follow-up Observations

We observed the SNe presented in this work (Table 1) in X-rays with Swift/XRT (D. N. Burrows et al. 2005) as part of our Guest Investigator programs (PI: Corsi). X-ray observations of SN 2020jqm and SN 2021ywf were already presented in A. Corsi et al. (2023).

We analyze the multiple Swift/XRT observations per source (number of observations per source: SN 2020jqm three, SN2022xzc one, SN 2022crr two, SN 2022xxf 10, SN 2023eiw four, SN 2023zeu four, SN 2024rjw six, SN 2024abup 12, SN 2024adml nine) using the online XRT tools as described in P. A. Evans et al. (2009). For count rate to flux conversion, we adopt a power-law model with photon index $\Gamma = 2$, and correct for Galactic absorption. We do not detect any X-ray emission for any of the SNe in our sample. We summarize our 3σ upper limits in Table 3, and discuss the implications in Section 3.4.

2.4. Radio Follow-up Observations

We carried out VLA observations of the SNe in our sample under several observing programs (PI: Corsi). The results are presented in Table 4.

The VLA data were calibrated in `CASA` (J. P. McMullin et al. 2007) using the automated VLA calibration pipeline. Manual inspection was conducted for additional radio-frequency interference identification and flagging. Calibrated images were formed using `tclean`. The `imstat` task was used on the residual images to derive rms noise values in circular regions centered at the optical position of each SN with radius 10× the full width at half-maximum (FWHM) of the nominal synthesized beam. We then used `imstat` on the clean images to estimate the maximum flux density within a circular region centered on the SN optical position, with a radius equal to the FWHM of the synthesized beam. We report an upper limit (or detection) when the maximum peak flux density in the region is $<3\sigma$ (or $\geqslant 3\sigma$). For detections, errors on the measured peak flux densities are the quadrature sum of the noise rms and a

[21] https://www.wiserep.org/

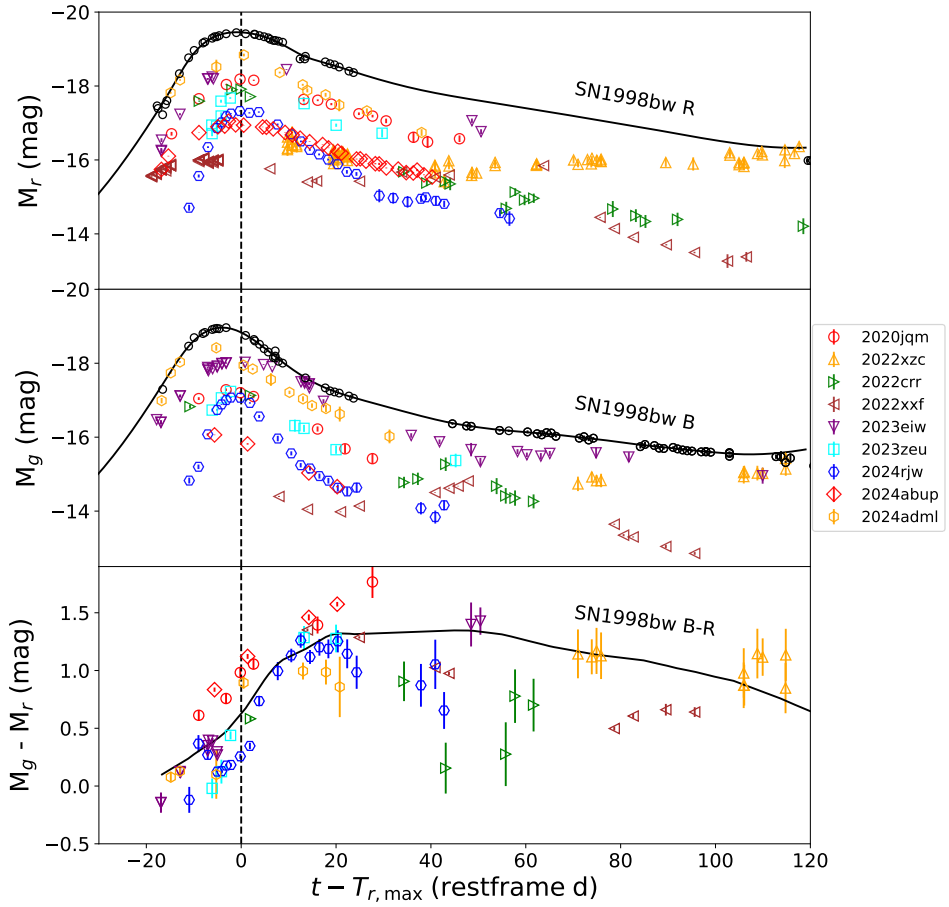

Figure 1. P48 *r*-band (top) and *g*-band (middle) light curves for the SNe in our sample, compared with the *R*- and *B*-band light curves of SN 1998bw, respectively. The bottom panel shows the corresponding color evolution, with the archetypal SN 1998bw represented by black open circles.

systematic absolute flux calibration error estimated as 5% of the peak flux density. All detections were also checked for extended versus pointlike morphology using the `imfit` task. Resolved detections are marked as such in Table 4.

3. Multiwavelength Analysis

3.1. Photospheric Velocities

We confirm the Type Ic-BL classification of each object in our sample by measuring their photospheric velocities ($v_{\rm ph}$). SNe Ic-BL are characterized by high expansion velocities, which manifest as line broadening in their spectra. A good proxy for the photospheric velocity is that derived from the maximum absorption position of Fe II λ5169 (e.g., M. Modjaz et al. 2016). In practice, we estimate the Fe II line velocity by comparing it to an average SN Ic spectral template. We caution that estimating this velocity is not easy given the strong line blending. We first preprocessed one high-quality spectrum per object using the IDL routine `WOMBAT`, then smoothed the spectrum using the Python-based routine `SESNspectraPCA`,[22] and finally ran `SESNSpectraLib` (Y.-Q. Liu et al. 2016; M. Modjaz et al. 2016) to obtain final velocity estimates. Measured values for the photospheric velocities, their errors at 84% confidence (1σ single-sided), and the rest-frame phase in days since maximum *r*-band light of the spectra used to measure them are also reported in Table 2.

In Figure 3, we show a comparison of the photospheric velocities estimated for the SNe in our sample with those derived from spectroscopic modeling for a number of SNe Ic. Our measured velocities are consistent, within measurement errors, with those from the previous ZTF SN Ic-BL sample (A. Corsi et al. 2023) and the Palomar Transient Factory (PTF)/iPTF sample (F. Taddia et al. 2019).

The photospheric-phase spectrum available for SN2024adml (ZTF24abwsaxu) is very low resolution and poor quality, resulting in higher uncertainty on the velocity estimate. For SN 2022xzc, we were unable to obtain estimated velocities as the spectra show features akin to a SN Ic rather than a SN Ic-BL, and `SESNSpectraLib` is designed only to measure the spectra of SNe Ic-BL.

3.2. Bolometric Light-curve Analysis

We derive the bolometric light curves of the SNe in our sample using the `haffet` framework (S. Yang & J. Sollerman 2023), which we describe below. First, we correct all ZTF photometry for Galactic extinction, using the Milky Way color excess $E(B-V)_{\rm MW}$ toward the positions of the SNe (E. F. Schlafly & D. P. Finkbeiner 2011). All reddening corrections are applied using the J. A. Cardelli et al. (1989) extinction law with $R_V = 3.1$. We then interpolate our P48 forced-photometry light curves using a Gaussian process (GP) via the `GEORGE`[23] package. SNe of the same type are expected

[22] https://github.com/metal-sn/SESNspectraPCA

[23] https://george.readthedocs.io/en/latest/

Table 2
Optical Properties of the Nine SNe in Our Sample

SN	$T_{r,\max}$ (MJD)	$M_r^{\rm peak}$ (AB mag)	$M_g^{\rm peak}$ (AB mag)	T_0-$T_{r,\max}$ (days)	$M_{\rm Ni}$ ($M_\odot$)	τ_m (days)	$v_{\rm ph}$[a] (10^4 km s^{-1})	$M_{\rm ej}$ ($M_\odot$)	$E_{\rm k}$ (10^{51} erg)
2020jqm	58996.27	-18.19 ± 0.02	-17.28 ± 0.03	$-17.4^{+1.5}_{-1.5}$	$0.36^{+0.01}_{-0.01}$	$20.15^{+0.55}_{-0.50}$	1.3 ± 0.3 (-0.5)	5.6 ± 1.3	5.6 ± 2.9
2022xzc	60061.48	-16.64 ± 0.02	-15.93 ± 0.08	$-224.1^{+32.2}_{-32.2}$	…	$19.18^{+0.13}_{-0.15}$	…	…	…
2022crr	59637.50	-17.94 ± 0.03	-17.42 ± 0.14	$-12.8^{+0.5}_{-0.5}$	$0.18^{+0.01}_{-0.01}$	$7.28^{+0.34}_{-0.40}$	1.5 ± 0.2 (3.0)	0.8 ± 0.1	1.1 ± 0.3
2022xxf	59950.53	-15.69 ± 0.06	-15.25 ± 0.02	$-80.0^{+0.1}_{-0.1}$	…	$10.17^{+0.15}_{-0.20}$	1.5 ± 0.2 (-4.0)	1.7 ± 0.2	2.2 ± 0.7
2023eiw	60059.20	-18.45 ± 0.02	-18.41 ± 0.08	$-28.4^{+0.4}_{-0.4}$	$0.43^{+0.01}_{-0.01}$	$20.36^{+0.49}_{-0.21}$	1.4 ± 0.5 (-8.0)	6.3 ± 2.3	7.4 ± 5.9
2023zeu	60295.20	-17.82 ± 0.12	-17.31 ± 0.14	$-9.5^{+1.5}_{-1.5}$	$0.19^{+0.01}_{-0.01}$	$7.60^{+0.17}_{-0.13}$	1.9 ± 0.5 (-6.0)	1.2 ± 0.3	2.5 ± 1.5
2024rjw	60536.32	-17.32 ± 0.01	-17.09 ± 0.04	$-12.2^{+0.2}_{-0.1}$	$0.11^{+0.01}_{-0.01}$	$8.65^{+0.18}_{-0.21}$	1.7 ± 0.5 (-2.0)	1.3 ± 0.4	2.3 ± 1.5
2024abup	60651.36	-17.05 ± 0.01	-16.52 ± 0.04	$-20.7^{+0.4}_{-0.3}$	$0.10^{+0.01}_{-0.01}$	$20.31^{+0.42}_{-0.68}$	0.8 ± 0.1 (28.0)	$<3.4 \pm 0.5$	$>1.3 \pm 0.4$
2024adml	60666.50	-18.82 ± 0.04	-18.40 ± 0.10	$-21.8^{+0.5}_{-0.4}$	$0.41^{+0.01}_{-0.01}$	$13.81^{+0.62}_{-0.65}$	0.8 ± 0.6 (2.0)	1.5 ± 1.2	0.6 ± 1.0

Notes. From left to right, we list the SN name; the MJD of maximum light in the r band; the absolute magnitude at r-band peak; the absolute magnitude at g-band peak; the estimated explosion time in days since r-band maximum; the estimated nickel mass; the characteristic timescale of the bolometric light curve; the photospheric velocity; the ejecta mass; and the kinetic energy of the explosion. We note that the Arnett model cannot be used on the double-peaked light curves of SN 2022xxf and SN 2022xzc; see Section 3.2 for more details. The optical properties of SN 2020jqm were previously discussed in A. Corsi et al. (2023); see Sections 3.1 and 3.2 for discussion. All times are reported in the rest frame.
[a] Rest-frame phase days of the spectrum used to measure the velocity.

to exhibit similar intrinsic spectral energy distribution (SED) evolution in their early phases. As shown in the bottom panel of Figure 1, all SNe in our sample display very similar early-phase (i.e., 10 rest-frame days after maximum light) $g - r$ colors as SN 1998bw, suggesting minimal influence from host-galaxy extinction. Therefore, we do not account for host-galaxy extinction in this study. We then calculate $g - r$ colors using GP-interpolated light curves and derive bolometric light curves by applying the empirical relations from J. D. Lyman et al. (2014, 2016), which provide bolometric corrections based on $g - r$ color measurements.

We fit the constructed bolometric light curves with the semi-analytic models developed by W. D. Arnett (1982), which relate the light-curve properties to the nickel mass ($M_{\rm Ni}$), the characteristic timescale (τ_m), and the time interval between explosion (T_{exp}) and peak (e.g., $T_{\max}$) epoch (see Table 2). We note that the Arnett model assumes a SN is powered solely by radioactive decay. Hence, this model may not fully capture the physics of SNe Ic-BL that host a central engine. Nonetheless, previous work (e.g., F. Taddia et al. 2019) has shown that the optical light curves of most SNe Ic-BL are well reproduced by ^{56}Ni-powered models, with inferred average parameters ($M_{\rm Ni}$, $M_{\rm ej}$, and E_k) that are, within uncertainties, consistent with those of GRB SNe. Accordingly, we adopt the Arnett model here, with the caveat that in the presence of a central engine the parameter values inferred from the Arnett model should be interpreted as effective descriptors of the light-curve behavior, rather than as a fully accurate representation of the underlying explosion physics.

Because of the sparsity of early-time observations in our sample, power-law fits aimed at determining the time of first light result in poor constraints. Hence, we adopt the Arnett model to estimate the explosion time, using the GP-inferred peak epoch as a reference. This method is applicable primarily to SNe with a single, dominant peak in their light curves. As shown in Figures 4 and 5, two sources in our sample (SN 2022xxf and SN 2022xzc) exhibit double-peaked light curves (see Y. Sharma et al. 2025). In such cases, the Arnett model fit cannot be used to estimate the nickel masses or explosion times. In fact, when Arnett modeling was attempted on 2022xxf's first peak, the estimated explosion date returned was after the date of optical discovery. Therefore, we set the explosion epoch as the midpoint between the last nondetection prior to discovery and the first confirmed detection.

Next, using the measured characteristic timescale τ_m of the bolometric light curve and the photospheric velocities estimated from spectral fitting (see Section 3.1), we derive the ejecta mass ($M_{\rm ej}$) and the kinetic energy (E_k) via the following relations (see, e.g., Equations (1) and (2) in J. D. Lyman et al. 2016):

$$\tau_m^2 v_{\rm ph,max} = \frac{2\kappa}{13.8c} M_{\rm ej}, \quad v_{\rm ph,max}^2 = \frac{5}{3}\frac{E_k}{M_{\rm ej}}. \tag{1}$$

We assume a constant effective optical opacity of $\kappa = 0.07$ g cm^{-2}. Using κ as a constant is justified if electron scattering is the dominant opacity source (R. A. Chevalier 1992). As discussed in Z. Cano (2013), various works have adopted values of κ in the range 0.05–0.08 g cm^{-2}. The ejecta mass and kinetic energy depend on κ through the diffusion-time relation (Equation (1)), such that $M_{\rm ej} \propto \kappa^{-1}$ and $E_k \propto M_{\rm ej} v_{\rm ph}^2 \propto \kappa^{-1}$. Accordingly, the values reported in Table 2 would be modified by factors of ∼0.88–1.4 over the 0.05–0.08 g cm^{-2} range.

We note that to derive $M_{\rm ej}$ and E_k as described above we assume the photospheric velocity evolution is negligible within 15 days relative to the peak epoch, and use the spectral velocities measured within this time frame to estimate $M_{\rm ej}$ and E_k in Equation (1) (see Table 2).

For all SNe in our sample for which we are able to measure photospheric velocities, we report the Table 2 median ejecta masses and kinetic energies of $1.6 \pm 0.6\,M_\odot$ and $2.3 \pm 0.8 \times 10^{51}$ erg, respectively. These values are most compatible with those of $1.7\,M_\odot$ and 2.2×10^{51} erg, reported in A. Corsi et al. (2023), and close to the median values of $1.4\,M_\odot$ and 2.1×10^{51} erg, reported in G. P. Srinivasaragavan et al. (2024). Our median values are both a factor of ≈2 smaller than those of $3.1\,M_\odot$ and 5.1×10^{51} erg, reported in F. Taddia et al. (2019). We note that SN 2023eiw has the highest $M_{\rm ej} = 6.3 \pm 2.3\,M_\odot$,

Table 3
Swift/XRT Observations

SN	T_{XRT} (MJD)	$T_{XRT}-T_{exp}$ (days)	Exp. (ks)	$F_{0.3-10\ keV}$ (10^{-14} erg cm^{-2} s^{-1})	$L_{0.3-10keV}$ (10^{40} erg s^{-1})
2020jqm	59002.09	23 ± 1.5	7.4	<3.3	<11
2022xzc	59903.00	34 ± 0.1	7.4	<4.0	<6.7
2022crr	59640.46	13 ± 0.02	3.3	<30	<24
2022xxf	59882.11	6.2 ± 0.2	34	<2.2	$<4.4 \times 10^{-2}$
2023eiw	60061.25	29 ± 0.4	12	<3.2	<4.7
2023zeu	60292.12	5.2 ± 1.7	16	<2.4	<5.0
2024rjw	60537.07	12 ± 1.5	11	<1.7	<1.6
2024abup	60636.80	0.45 ± 0.4	27	<2.5	$<1.9 \times 10^{-1}$
2024adml	60656.30	$6.1\pm^{0.3}_{0.2}$	27	<1.3	<4.1

Note. From left to right, we list the SN name; the start of the observation (in MJD); the epoch between the XRT observation and the estimated SN explosion (in days), with error (which is dominated by the uncertainties on the estimated SN explosion time); the XRT exposure time;and the 0.3–10 keV unabsorbed flux and luminosity obtained by coadding all observations (and 3σ upper limit for nondetections).

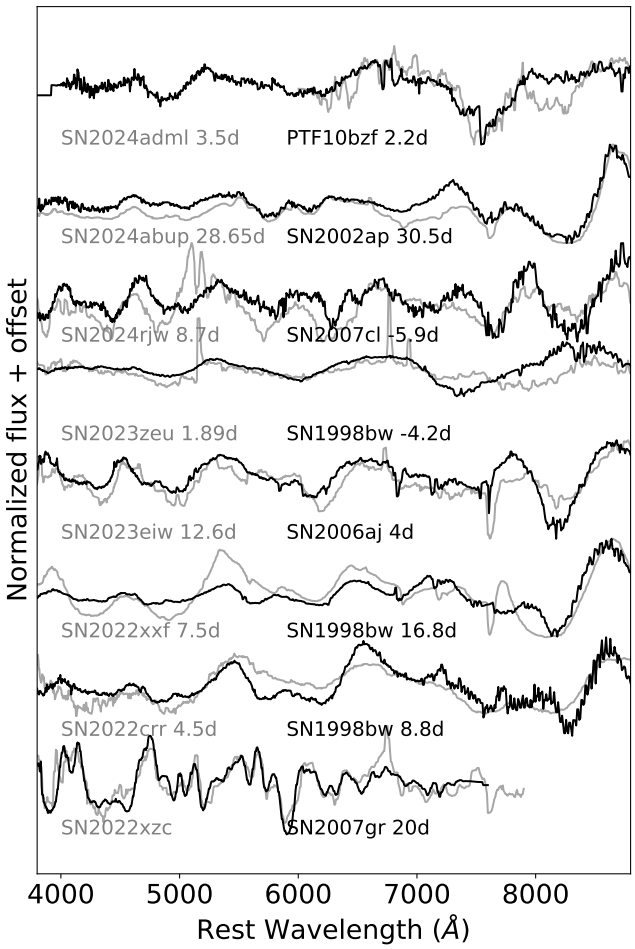

Figure 2. This plot displays the spectra (in gray) along with their best-matching templates (in black) from `Astrodash` for the SNe Ic-BL in our sample. The spectra are labeled with their IAU designation, the IAU name of the best-matching SN, and their phases. Note that for SN 2022xzc, we do not show the phase since the explosion time is hard to estimate due to its peculiar light curve. The spectra shown here are the highest-resolution observations obtained during the photospheric phase.

$E_k = (7.4 \pm 5.9) \times 10^{51}$ erg, which skews the overall mean of sources in Table 2; without its values the mean of this table becomes comparable to its median, at $M_{ej} = 1.65\,M_\odot$ and $E_k = 1.67 \times 10^{51}$ erg.

3.3. Search for Gamma-Rays

Based on the explosion dates derived in Section 3.2 (see also Table 2), we searched for coincident GRBs using the Burst Alert Telescope (BAT) on board the Neil Gehrels Swift Observatory (N. Gehrels et al. 2004; S. D. Barthelmy et al. 2005), the Gamma-Ray Burst Monitor (GBM) on board Fermi (C. Meegan et al. 2009), and the Konus instrument on board the NASA Wind spacecraft. We did not include SN 2022xzc or SN 2022xxf in the searches, given their uncertain explosion dates (Section 3.2).

No spatial and temporal coincidences were identified with GRBs detected by the BAT or GBM. Several temporal coincidences were found with GRBs detected by Konus/Wind, particularly for SN 2020jqm, SN 2023zeu, and SN 2024abup. However, these are the three events with the least precise explosion date constraints in our sample, and given the search window and the rate of Konus/Wind detections (∼0.5 per day), we expect multiple temporal coincidences by chance. Thus, we cannot robustly associate any of the SNe Ic-BL in our sample with known GRBs.

3.4. X-Ray Constraints

None of the SNe in our sample showed evidence for significant X-ray emission in data collected using Swift/XRT (see Section 2.3). In Table 3, we report the 0.3–10 keV flux upper limits (90% confidence) derived after correcting for Galactic absorption (R. Willingale et al. 2013). In Figure 6, we show these upper limits (downward-pointing triangles) compared with the X-ray observations of GRB-associated SNe. We can exclude X-ray emission as faint as the afterglow of the low-luminosity GRB 980425 (SN 1998bw) for three of the SNe Ic-BL in our sample (SN 2024rjw, SN 2024abup, and SN 2022xxf). Our X-ray observations also exclude GRB 060218 (SN 2006aj)-like emission for SN 2022xxf, SN 2023zeu, SN 2024rjw, and SN 2024abup. As we discuss in the next section, while our radio observations can rule out GRB 980425 (SN 1998bw)-like emission for all SNe in our sample (Figure 7), these X-ray upper limits are unsurpassed in terms of the constraints set on GRB 060218 (SN 2006aj)-like ejecta for the SNe in our sample. This highlights the value of prompt Swift/XRT observations for nearby SNe, especially given the challenges in obtaining prompt VLA follow-up. We can also compare our X-ray upper limits with predictions for a range of off-axis GRB afterglow models derived using

`afterglowpy` (dashed lines in Figure 6; G. Ryan et al. 2020). All together, our Swift/XRT observations rule out GRB X-ray afterglows with kinetic energies $E \gtrsim 10^{51}$ erg viewed slightly off-axis $\theta_{\rm obs} \approx (2.5\text{–}3.5)\theta_j$. For the most nearby events (SN 2022xxf and SN 2024abup), our upper limits also exclude slightly off-axis jets with kinetic energies as low as $\approx 10^{49}$–10^{50} erg.

We note that these constraints depend on the choice of the microphysical parameters ϵ_e and ϵ_B, with the most critical dependence being on ϵ_e. Specifically, decreasing ϵ_e by an order of magnitude while keeping the other parameters unchanged would shift the model light curves down by an order of magnitude or more. On the other hand, a change in ϵ_B has a very small effect. We also assume a constant-density interstellar medium (ISM). A stellar wind medium with a density profile $\rho \propto R^{-2}$ would impact off-axis light-curve predictions. Generally speaking, for off-axis observers, a wind medium correlates with a shallower rise to the peak of the light curve, and a flatter and wider light-curve peak. However, this effect is less pronounced in X-rays (compared to, e.g., the optical or radio), since above the cooling synchrotron break the observed flux density becomes much less sensitive to the external density (see, e.g., J. Granot et al. 2018; X.-H. Zhao & K.-F. Cheng 2022, for a discussion).

3.5. Radio Constraints

As shown in Table 4, we obtained confident radio detections ($>3\sigma$ level) for seven SNe in our sample. Four of these seven (SN 2022xzc, SN 2023zeu, SN 2024abup, SN 2024adml) are associated with emission that is likely dominated by host-galaxy light (see Figures 8–11). The remaining three are radio detections most likely associated with genuine SN radio counterparts.

As evident from Figure 7, none of the SNe in our sample for which we can exclude radio emission dominated by host-galaxy light show evidence for SN 1998bw-like emission. The three events for which we have a radio counterpart detection (SN 2020jqm and SN 2022xxf, both of Type Ic-BL, and SN 2024rjw, a Type Ic) suggest the presence of either mildly relativistic ejecta or strong interaction with a dense circumstellar medium (CSM). As described in more detail below, SN 2022xxf has a double-peaked optical light curve (Figure 4) indicative of CSM interaction. However, the radio observations do not provide evidence for strong CSM interaction, but rather suggest the presence of mildly relativistic ejecta. SN 2020jqm is a double-peaked SN Ic-BL with *C*-band detections presented in A. Corsi et al. (2023). SN 2024rjw appears pointlike in our images and shows a late-time rise in flux. While it has been reclassified as a Type Ic SN, we retain it in the sample due to its strong radio emission and light-curve behavior, indicative of a dense CSM interaction similar to SN 2020jqm (A. Corsi et al. 2023) and PTF11qcj (N. T. Palliyaguru et al. 2019).

We also analyzed pre- and postexplosion Quick Look images from the VLA Sky Survey (VLASS) for five of the SNe in our sample (SN 2020jqm, SN 2022xzc, SN 2022crr, SN 2022xxf, SN 2023eiw), and preexplosion images for four of our SNe (SN 2023zeu, SN 2024rjw, SN 2024abup, SN 2024adml). The VLASS images revealed no significant ($>3\sigma$) radio detections at the optical SN positions. This is not surprising, given that the VLASS rms sensitivity of $\approx$0.12 mJy at 3 GHz (A. C. V. Hernáandez & H. Andernach 2018; C. J. Law et al. 2018) is much shallower than that achieved via our deep VLA follow-up.

In what follows, we describe the constraints derived via our VLA observations in detail.

3.5.1. Host-galaxy-dominated Radio Emission

SN 2022xzc displays strong evolution in the observed radio flux across our two epochs. In our first observation, carried out with the VLA in its C configuration, there is evidence for extended emission at 5.5 GHz (Figure 8), with a $\approx 16 \pm 3\farcs4 \times 6 \pm 1\farcs5$ emitting region (derived using the `imfit` task in `CASA` within a circular region centered on the optical SN position with a radius of $3\farcs5$). The measured peak flux density of $\approx$47 μJy shows a large discrepancy with the integrated flux of $\approx$409 μJy, as expected in the case of extended emission. In our second epoch, carried out with the VLA in its B configuration, the emission appears to be resolved out, resulting in a nondetection within the searched area. We can estimate a lower limit on the host-galaxy star formation rate (SFR) required to account for the observed radio emission using the above measured integrated flux density and the following relation (E. J. Murphy et al. 2011):

$$\left(\frac{\rm SFR_{1.4\,GHz}}{M_\odot\,{\rm yr}^{-1}}\right) = 6.35 \times 10^{-29}\left(\frac{L_{\rm 1.4\,GHz}}{\rm erg\ s^{-1}Hz^{-1}}\right), \quad (2)$$

which implies SFR $\gtrsim 1\,M_\odot\,{\rm yr}^{-1}$ when extrapolating the 1.4 GHz flux from the observed value at $\nu_{\rm obs} = 5.5$ GHz, assuming a spectral index $\alpha = -0.7$, i.e.,

$$L_{\rm 1.4\,GHz} = 4\pi D_L^2 S_{\nu_{\rm obs}}\left(\frac{1.4\ {\rm GHz}}{\nu_{\rm obs}}\right)^{\alpha}(1+z)^{\alpha-1}, \quad (3)$$

where $S_{\nu_{\rm obs}}$ is the integrated radio flux as estimated for the host galaxy. The derived radio SFR value is broadly consistent with the value of $\approx 0.4\,M_\odot\,{\rm yr}^{-1}$ obtained from SED fitting to the NASA/IPAC Extragalactic Database (NED) host-galaxy photometry. We caution that, due to various degeneracies in the fit, as well systematics related to the inability to capture the full galaxy light in the photometry of nearby objects, all optical SFRs quoted hereafter are only accurate to about a factor of $\approx$3.

In the case of SN 2023zeu, we measure a constant radio flux density over two epochs spanning more than 500 days postexplosion (see Table 5). The detected radio emission in the C configuration (Figure 9) is resolved at 5.5 GHz, with a beam-deconvolved size of $7\farcs06 \pm 1\farcs1 \times 0\farcs87 \pm 0\farcs87$ (derived using the `imfit` task in `CASA` within a circular region centered on the optical SN position with a radius of $3\farcs5$). This epoch displays a peak flux density and an integrated flux density of $\approx$36 and $\approx$66 μJy, respectively. The estimated radio SFR is $\gtrsim 0.2\,M_\odot\,{\rm yr}^{-1}$, broadly compatible with that obtained from the optical host-galaxy light ($\approx 0.1\,M_\odot\,{\rm yr}^{-1}$).

For SN 2024abup, our first two $\approx$5 GHz observations, carried out (at $\approx$22 days and $\approx$52 days since explosion) with the VLA in its most extended A configuration, did not yield a radio detection at 5 GHz. However, strong radio emission was detected at the same frequency with the VLA in its C configuration. The emission measured within a circular region of radius $3\farcs5$ centered on the optical SN position is extended (Figure 10), with an estimated size of $\approx 46 \pm 0\farcs64 \times 10 \pm 0\farcs18$.

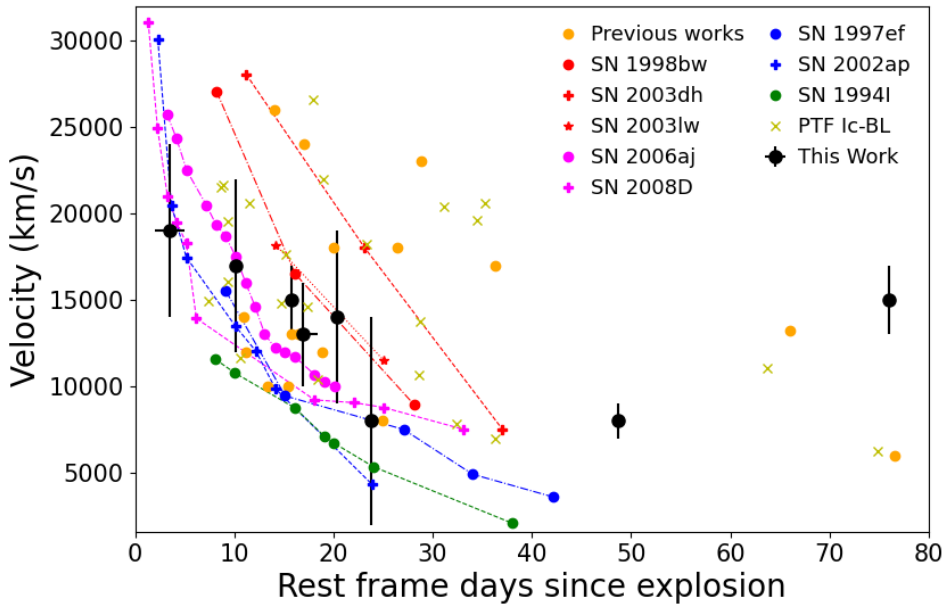

Figure 3. Photospheric velocities of the seven Ic-BL and one Ic (2024rjw) ZTF SNe within our sample (black) plotted as a function of time since explosion (see Table 2). Velocities are measured using Fe II 5169 Å. We also plot the photospheric velocities of GRB SNe (red; K. Iwamoto et al. 1998; P. A. Mazzali et al. 2003, 2006a),X-ray flash/X-ray transient SNe (magenta; P. A. Mazzali et al. 2006b; E. Pian et al. 2006; M. Modjaz et al. 2009), SNe Ic-BL (blue; P. A. Mazzali et al. 2000, 2002), and Type Ic SNe (green; D. N. Sauer et al. 2006). The velocities for the SNe Ic-BL in A. Corsi et al. (2016) and F. Taddia et al. (2019) are shown as yellow crosses, and those from A. Corsi et al. (2023) and G. P. Srinivasaragavan et al. (2024) as orange dots.

The measured peak flux density is $\approx 232\,\mu$Jy, while the integrated flux density is ≈ 6 mJy. This implies a radio SFR of $\approx 0.7\,M_\odot\,\mathrm{yr}^{-1}$ (assuming the spectral index adopted above). Estimating the SFR of the host galaxy of SN 2024abup from optical light is challenging because its large angular size makes NED photometric estimates unreliable. We obtain an order-of-magnitude estimate of $\approx 0.2\,M_\odot\,\mathrm{yr}^{-1}$ using the NED-reported Hα flux. However, this estimate does not account for dust correction, and given the visible dust lane, the optical SFR estimate is likely higher by a factor of a few higher (and hence compatible with the radio estimate).

Finally, the first two 5.5 GHz observations of SN 2024adml with the VLA in its A configuration (at ≈ 9 and ≈ 34 days since explosion) did not show evidence for significant radio emission (see Table 4). However, our third observation, conducted at ≈ 181 days postexplosion with the VLA in its C configuration, shows extended radio emission (Figure 11) of size $\approx 10 \pm 0\farcs51 \times 7\farcs7 \pm 0\farcs35$ (derived using the `imfit` task in `CASA` within a circular region of radius $3\farcs5$ around the optical SN position). The measured peak flux density is $\approx 68\,\mu$Jy, while the integrated flux density is $\approx 450\,\mu$Jy. This implies an SFR of $\approx 2\,M_\odot\,\mathrm{yr}^{-1}$, compared to $\approx 0.4\,M_\odot\,\mathrm{yr}^{-1}$ obtained from optical SED modeling.

3.5.2. Properties of the Radio-emitting Ejecta

Here, we constrain the physical properties of the radio-emitting ejecta in the SNe with radio detections not associated with host-galaxy light, within the synchrotron self-absorption (SSA) model for radio SNe (R. A. Chevalier 1998). In this model, the measured radio peak frequency and flux provide estimates of the emitting region's size (and hence its velocity), as well as the progenitor's mass-loss rate. Starting from

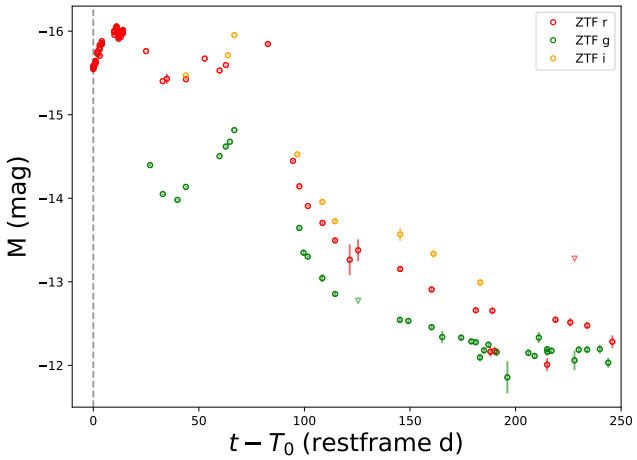

Figure 4. The *g*-, *r*-, and *i*-band light curves of SN 2022xxf, with data points shown as circles (green, red, and orange, respectively) and upper limits marked as downward triangles. The light curve clearly displays a double-peaked structure. The vertical dashed line indicates the estimated explosion epoch. See H. Kuncarayakti et al. (2023) for further discussion of the interpretation of this double-peaked light curve in the context of ejecta–CSM interaction as a plausible explanation for the second light-curve hump.

Equations (11) and (13) of R. A. Chevalier (1998):

$$R_p \approx 8.8 \times 10^{15}\,\mathrm{cm}\left(\frac{\eta}{2\alpha}\right)^{1/(2p+13)}\left(\frac{F_p}{\mathrm{Jy}}\right)^{(p+6)/(2p+13)} \times \left(\frac{d_L}{\mathrm{Mpc}}\right)^{(2p+12)/(2p+13)}\left(\frac{\nu_p}{5\ \mathrm{GHz}}\right)^{-1}, \quad (4)$$

where $\alpha \approx 1$ is the ratio of relativistic electron energy density to magnetic energy density, F_p is the flux density at the SSA peak, ν_p is the SSA frequency, and R/η is the thickness of the

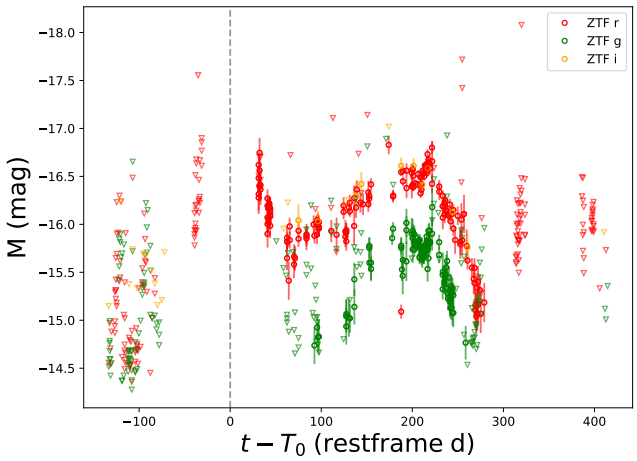

Figure 5. The *g*-, *r*-, and *i*-band light curves for SN 2022xzc, pointing to a double-peaked structure.

radiating electron shell, with $\eta \equiv f^{-1}$ the inverse of the filling factor f of the synchrotron-emitting region (R. A. Chevalier 1998; A. M. Soderberg et al. 2005).

By setting $R_p \approx \nu_s t_p$ in Equation (4) and using $L_p \approx 4\pi d_L^2 F_p$, we derive

$$\left(\frac{L_p}{\mathrm{erg\ s^{-1}\ Hz^{-1}}}\right) \approx 1.2 \times 10^{27} \left(\frac{\beta_s}{3.4}\right)^{(2p+13)/(p+6)} \times \left(\frac{\eta}{2\alpha}\right)^{-1/(p+6)} \left(\frac{\nu_p}{5\ \mathrm{GHz}} \frac{t_p}{1\ \mathrm{day}}\right)^{(2p+13)/(p+6)}, \quad (5)$$

where $\beta_s = \nu_s/c$. In Figure 12, we plot this relation for various values of β_s, assuming $p = 3$, $\eta = 2$, and $\alpha = 1$. We note that η is typically assumed to be in the range 2–10 (R. A. Chevalier 1998; A. M. Soderberg et al. 2005). Adopting different values of η in this range would change our estimates by $\lesssim$10%. Relativistic events like SN 1998bw lie above the $\beta_s \gtrsim 1$ regime, outside the validity of the nonrelativistic assumptions in these equations.

To estimate the speed of the radio-emitting ejecta for the three SNe in our sample with radio detections, we apply Equation (4) using our observed values and plot the results in Figure 12. For sources whose peak flux occurs at the first epoch of observation, we mark them with arrows to indicate that the true peak may lie at earlier times (i.e., further to the left on the plot).

SN 2020jqm (Ic-BL) and SN 2024rjw (Ic) both exhibit ejecta speeds $\lesssim 0.5c$ and show late-time peaking radio emission compatible with strong circumstellar interaction (Figure 12), similar to that observed in other SNe Ic-BL (e.g., A. Corsi et al. 2014) and Ib/c events (e.g., S. Wellons et al. 2012). As discussed below, this interpretation is reinforced by the inferred progenitor mass-loss rates.

We can also estimate the progenitor's mass-loss rate using SSA theory. From Equations (12) and (14) of R. A. Chevalier (1998), the magnetic field is

$$B_p \approx 0.58\ \mathrm{G} \left(\frac{\eta}{2\alpha}\right)^{4/(2p+13)} \left(\frac{F_p}{\mathrm{Jy}}\right)^{-2/(2p+13)} \times \left(\frac{d_L}{\mathrm{Mpc}}\right)^{-4/(2p+13)} \left(\frac{\nu_p}{5\ \mathrm{GHz}}\right). \quad (6)$$

Assuming the shock expands into a CSM with density

$$\rho \approx 5 \times 10^{11}\ \mathrm{g\ cm^{-3}}\, A_*\, R^{-2}, \quad (7)$$

where a fraction ϵ_B of the energy density ρv_s^2 goes into magnetic fields, we obtain

$$\frac{B_p^2}{8\pi} = \epsilon_B \rho \nu_s^2 = \epsilon_B \rho R_p^2 t_p^{-2}. \quad (8)$$

Solving for L_p yields

$$\left(\frac{L_p}{\mathrm{erg\ s^{-1}\ Hz^{-1}}}\right) \approx 1.2 \times 10^{27} \left(\frac{\eta}{2\alpha}\right)^2 \left(\frac{\nu_p}{5\ \mathrm{GHz}} \frac{t_p}{1\ \mathrm{day}}\right)^{(2p+13)/2} \times (5 \times 10^3 \epsilon_B A_*)^{-(2p+13)/4}. \quad (9)$$

In Figure 12, we overlay this relation with green dashed lines for various $\dot{M}$ values, assuming $p = 3$, $\eta = 2$, $\alpha = 1$, $\epsilon_B = 0.33$, and $v_w = 1000\ \mathrm{km\ s^{-1}}$. We find that relativistic events such as SN 1998bw favor lower inferred mass-loss rates, while CSM-interacting events such as PTF 11qcj, SN 202jqm, and SN 2024rjw favor larger mass-loss rates. While Equation (8) depends on assumed values for η, ϵ_B, and v_w, the trend in $\dot{M}$ holds across typical parameter choices.

Finally, we estimate the energy coupled to the fastest ejecta using (A. M. Soderberg et al. 2006a)

$$E_r \approx \frac{4\pi R_p^3}{\eta} \frac{B_p^2}{8\pi\epsilon_B} = \frac{R_p^3}{\eta} \frac{B_p^2}{2\epsilon_B}. \quad (10)$$

In Table 5, we summarize the derived properties for the two detected radio SNe (SN 2022xxf, SN 2024rjw); SN 2020jqm was covered in A. Corsi et al. (2023). All events show evidence for energies in the radio-emitting ejecta (and progenitor mass-loss rates) that are significantly lower (higher) than those of GRB SNe such as SN 1998bw ($\dot{M} \approx 2.5 \times 10^{-7} M_\odot\ \mathrm{yr^{-1}}$, $E_r \approx (1-10) \times 10^{49}$ erg; Z.-Y. Li & R. A. Chevalier 1999), SN 2009bb ($\dot{M} \approx 2 \times 10^{-6} M_\odot\ \mathrm{yr^{-1}}$, $E_r \approx 1.3 \times 10^{49}$ erg; A. M. Soderberg et al. 2010), and GRB 100316D (SN 2010bh; $\dot{M} \approx (0.4 - 1) \times 10^{-5} M_\odot\ \mathrm{yr^{-1}}$, $E_r \approx (0.3-4) \times 10^{49}$ erg; R. Margutti et al. 2013).

3.5.3. The Rate of SN 1998bw-like SNe Ic-BL

SNe Ic-BL constitute about 5% of all core-collapse SNe (W. Li et al. 2011; I. Shivvers et al. 2017). Based on the ZTF sample, we are beginning to constrain the rates of the brightest Ic-BL events with greater accuracy. Specifically, we derive volumetric rates of $\approx$80–200 $\mathrm{Gpc^{-3}\ yr^{-1}}$ for events with peak *r*-band absolute magnitudes in the range $-19\ \mathrm{mag} \leqslant M_r < -18.5$ mag, and $\approx$25–90 $\mathrm{Gpc^{-3}\ yr^{-1}}$ for events with $M_r < -19$ mag. Because the median peak absolute magnitude of the SNe in our sample is $M_r = -17.82$, and only one SN in our sample falls in the $M_r < -18.5$ range, hereafter we adopt a cumulative volumetric rate of SNe Ic-BL of $\approx$740–2600 $\mathrm{Gpc^{-3}\ yr^{-1}}$, based on the whole ZTF sample (D. Perley et al. 2026, in preparation).

The most stringent constraints on the rate of 1998bw-like events among SNe Ic-BL were set by A. Corsi et al. (2023), who showed that 1998bw-like events (defined here as events with radio emission observationally similar to SN 1998bw) constitute less than 19% of the SN Ic-BL population (at 99.865% confidence). With the additional observations

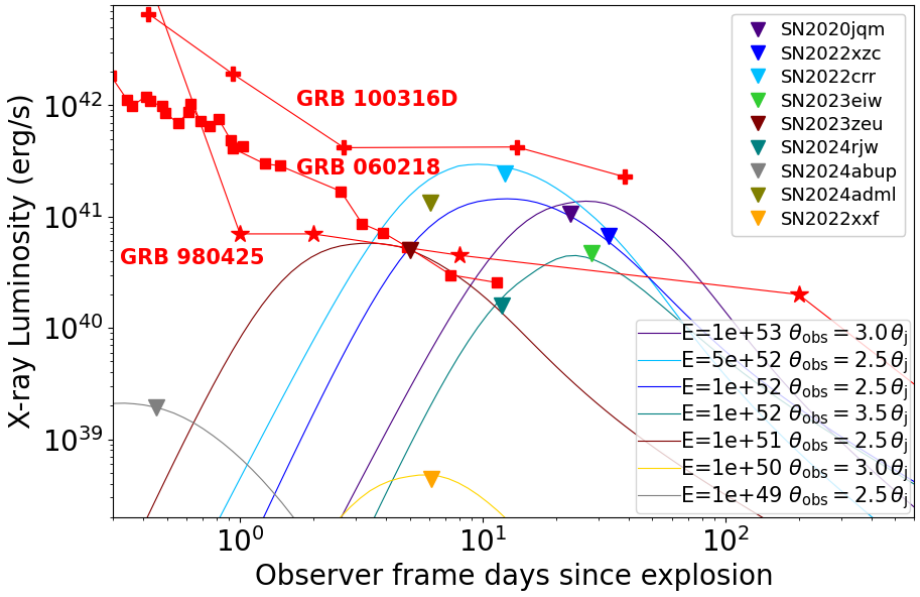

Figure 6. Swift/XRT upper limits (downward-pointing triangles) for the eight SNe Ic-BL and for the Type Ic SN 2024rjw in our sample, compared with the X-ray light curves of three low-luminosity GRBs. We can exclude X-ray emission as faint as the afterglow of the low-luminosity GRB 980425 (SN 1998bw) for SN 2024rjw, SN 2024abup, and SN 2022xxf. We also exclude GRB 060218 (SN 2006aj)-like emission for SN 2022xxf, SN 2023zeu, SN 2024rjw, and SN 2024abup. We can compare our X-ray upper limits with predictions for a range of off-axis GRB afterglow models derived using `afterglowpy` (dashed lines; G. Ryan et al. 2020). These models assume top-hat jets with isotropic-equivalent energies E, jet opening angles θ_j, and observers' viewing angles $\theta_{\rm obs}$, as indicated in the legend. We set $\epsilon_B = \epsilon_e = 0.1$, and use a constant-density ISM in the range $n = 1$–$50\ {\rm cm}^{-3}$. All together, our Swift/XRT observations rule out GRB X-ray afterglows with kinetic energies $E \gtrsim 10^{51}$ erg viewed slightly off-axis $\theta_{\rm obs} \approx (2.5$–$3.5)\theta_j$. For the most nearby events (SN 2022xxf and SN 2024abup), our upper limits also exclude slightly off-axis jets with kinetic energies as low as $\approx 10^{49}$–10^{50} erg.

presented here—seven new SNe Ic-BL for which we can exclude radio emission observationally similar to SN 1998bw (GRB 980425; see Figure 7)—our sample of radio-monitored SNe Ic-BL increases to 41 in total. This lowers the 99.865% confidence upper limit on the fraction of 1998bw-like events to $<6.61/41 \approx 16\%$, corresponding to a volumetric rate of $R_{\rm 1998bw\text{-}like} < 118$–$416\ {\rm Gpc}^{-3}\ {\rm yr}^{-1}$. Note that we use the fact that the Poisson 99.865% confidence (or 3σ Gaussian equivalent for a single-sided distribution) upper limit on zero SNe compatible with SN 1998bw is ≈ 6.61.

If we assume that all or the majority of low-luminosity GRBs have radio luminosities comparable to that of SN 1998bw, we can use the observed rate of low-luminosity GRBs ($R_{\rm LLGRB}$) and our derived constraints on the rate of 1998bw-like events ($R_{\rm 1998bw\text{-}like}$) to infer the low-luminosity GRB beaming angle:

$$R_{\rm LLGRB} = (1 - \cos\theta) R_{\rm 1998bw-like}. \quad (11)$$

Hereafter, we adopt $R_{\rm LLGRB} \approx 164$–$325\ {\rm Gpc}^{-3}\ {\rm yr}^{-1}$ based on H. Sun et al. (2015) and E. Liang et al. (2007). Our upper limit of $R_{\rm 1998bw\text{-}like} < 118$–$416\ {\rm Gpc}^{-3}\ {\rm yr}^{-1}$ sets a lower limit on the beaming angle θ:

$$\cos\theta = 1 - \frac{R_{\rm LLGRB}}{R_{\rm 1998bw-like}} \lesssim 1 - \frac{164\ {\rm Gpc}^{-3}\ {\rm yr}^{-1}}{416\ {\rm Gpc}^{-3}\ {\rm yr}^{-1}}, \quad (12)$$

$$\theta \gtrsim 52\ {\rm deg}. \quad (13)$$

It is clear that our radio observations increasingly disfavor the hypothesis that all low-luminosity GRBs are associated with 1998bw-like fast ejecta. On the other hand, radio emission similar to SN 2006aj, associated with GRB 060218, cannot be excluded for most of the SNe Ic-BL in our sample (see Figure 7), and would require faster radio follow-up (A. Corsi et al. 2023). Indeed, the working assumption in our analysis is that low-luminosity GRBs constitute a class of relativistic explosions with relatively small beaming factors (E. Liang et al. 2007), and that SN 1998bw is observationally representative of the bulk properties of this class. Under these assumptions, their radio light curves are expected to be less affected by viewing-angle effects. However, if the majority of the low-luminosity GRB population exhibited radio light curves more akin to SN 2006aj i.e., significantly fainter and more rapidly evolving, our study would not be able to probe them.

We emphasize that a systematic approach to radio follow-up campaigns would be highly beneficial, providing a unique opportunity to tighten existing constraints to the point where SN 1998bw-like emission could be firmly excluded in all SNe Ic-BL. To illustrate this potential, we examined the ZTF Bright Transient Survey catalog (C. Fremling et al. 2020; D. A. Perley et al. 2020), which contains approximately 90 SNe Ic-BL with redshifts $z \lesssim 0.2$, detected between 2018 and 2025. If sufficient VLA observing time had been available to monitor each of these events with the same sensitivity as achieved in this work (i.e., $\approx 50\ \mu$Jy at 5σ for 6 GHz observations of sources at $z \lesssim 0.2$), the resulting upper limit on the fraction of 1998bw-like SNe Ic-BL could have been as low as $<6.61/90 \approx 7\%$, corresponding to an event rate of $R_{\rm 1998bw\text{-}like} \lesssim 180\ {\rm Gpc}^{-3}\ {\rm yr}^{-1}$. This value is comparable to the lowest estimates of the low-luminosity GRB rate (H. Sun et al. 2015), underscoring the importance of systematic, high-sensitivity radio follow-up for constraining the diversity of engine-driven explosions.

Table 4
VLA Observations

SN	$T_{\rm VLA}$ (MJD)	$\Delta T_{\rm VLA}$ (day)	ν (GHz)	F_ν (μJy)	Conf.	Nom. Beam (arcsec)	Image rms (μJy)	Project Code
2020jqm	58997.03	17	5.6	167 ± 12	C	3.5	8.4	SG0117[a]
	59004.03	24	5.6	293 ± 17	C	3.5	8.5	SG0117[a]
	59028.98	49	14	76 ± 11	B	0.42	9.8	20A-568[a]
			5.5	206 ± 14	B	1.0	10	
			3	132 ± 13	B	2.1	11	
	59042.95	63	14	60 ± 11	B	0.42	10	20A-568[a]
			5.5	197 ± 13	B	1.0	8.9	
			3	194 ± 17	B	2.1	14	
	59066.09	86	14	58 ± 10	B	0.42	9.7	20A-568[a]
			5.5	135 ± 12	B	1.0	9.8	
			3	117 ± 13	B	2.1	12	
	59088.03	108	14	99 ± 9.1	B	0.42	7.6	20A-568[a]
			5.5	159 ± 12	B	1.0	8.4	
			3	191 ± 20	B	2.1	16	
	59114.74	134	14	520 ± 28	B	0.42	9.5	20A-568[a]
			5.5	617 ± 32	B	1.0	9.8	
			3	393 ± 23	B	2.1	12	
	59240.37	260	5.5	704 ± 36	A	0.33	7.0	20B-149[a]
2022xzc	59902.61	33	5.5	46.6 ± 8.9[b]	C	3.5	8.5	SI1108[a]
	59976.30	107	5.5	$\lesssim$17	B	1.0	5.7	SI1108[a]
2022crr	59686.42	58	6	$\lesssim$9.6	A	0.33	3.2	22A-463[c]
2022xxf	59874.71	4.9	5.5	614 ± 32	C	3.5	9	SI1108[a]
	59902.65	33	5.5	163 ± 24	C	3.5	11	SI1108[a]
	59929.45	60	5.5	83 ± 9.7	C	3.5	9.7	SI1108[a]
	59888.69	19	15	77 ± 6.3	C	1.4	5.0	22B-311[a]
			9	152 ± 11	C	2.1	7.6	
			5.5	261 ± 18	C	3.5	13	
	59956.41	87	15	15.0 ± 4.8	C → B	0.42	4.7	22B-311[a]
			9	35 ± 7.1	C → B	0.60	5.2	
			5.5	61 ± 8.6	C → B	1.0	8.0	
	60068.11	198	15	$\lesssim$15	B	0.42	5.1	22B-311[a]
			9	$\lesssim$20	B	0.60	6.5	
			5.5	$\lesssim$21	B	1.0	7.1	
2023eiw	60061.10	28	5.5	$\lesssim$19	B	1.0	6.2	SS 192066[a]
	60074.02	41	5.5	$\lesssim$18	B	1.0	5.9	SS 192066[a]
	60831.03	797	5.5	$\lesssim$20	C	3.5	6.7	SS 192066[a]
2023zeu	60313.14	26	5.5	49 ± 7.9[b]	D	12	7.7	SS 192066[a]
	60839.72	553	5.5	36 ± 6.9[b]	C	3.5	6.6	SS 192066[a]
2024rjw	60543.14	18	5.5	430 ± 23	B	1.0	7.8	SS 203066[a]
	60579.07	54	5.5	2580 ± 130	BnA	0.33	10	SS 203066[a]
	60658.79	134	5.5	2408 ± 120	A	0.33	9.0	SS 203066[a]
2024abup	60658.07	22	5.5	$\lesssim$22	A	0.33	7.3	SS 203066[a]
	60687.97	52	5.5	$\lesssim$19	A	0.33	6.2	SS 203066[a]
	60831.56	195	5.5	231 ± 15[b]	C	3.5	9.6	SS 203066[a]
2024adml	60659.41	9.0	5.5	$\lesssim$19	A	0.33	6.2	SS 203066[a]
	60684.34	34	5.5	22 ± 6.8[b]	A	0.33	6.7	SS 203066[a]
	60831.08	181	5.5	68 ± 8.9[b]	C	3.5	8.2	SS 203066[a]

Notes. From left to right, we give the SN name; the mid-MJD of the observation; the rest-frame days since estimated explosion; the observing frequency; the flux density and 3σ upper limit; the VLA array configuration; the FWHM of the VLA nominal synthesized beam; the image rms; and the VLA observing project code.
[a] PI: Corsi.
[b] Emission likely dominated by the host galaxy (resolved, marginally resolved, or nuclear; see text for discussion).
[c] PI: Balasubramanian.

3.6. Off-axis Jets or Cocoons?

As evident from Figure 7, our radio follow-up campaigns seem to consistently exclude SN 1998bw-like radio emission for the majority of SNe Ic-BL. However, several events are as radio-loud as SN 1998bw but peak at much later times. SN 2024rjw, classified as a Type Ic SN and presented here for the first time, shows persistent radio brightness beyond 100

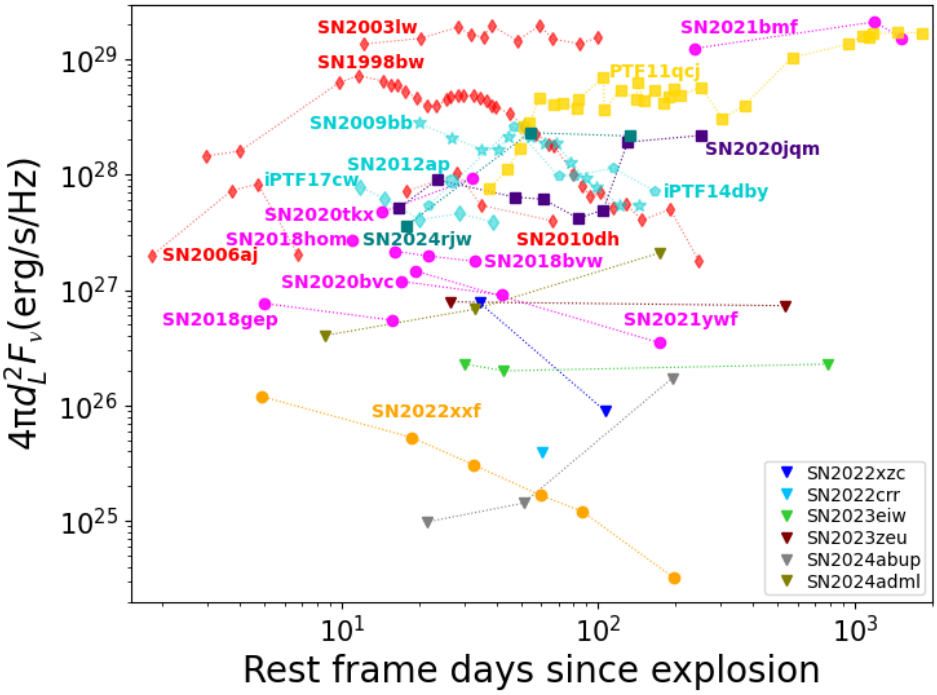

Figure 7. Radio (≈6 GHz) observations of the SNe Ic-BL in our sample (orange dots and squares for detections and downward-pointing triangles for upper limits; see Table 4). We compare these observations with the radio light curves of GRB SNe (red; S. R. Kulkarni et al. 1998; A. M. Soderberg et al. 2004; R. Margutti et al. 2013), relativistic-to-mildly relativistic SNe Ic-BL discovered independently of a gamma-ray trigger (cyan; A. M. Soderberg et al. 2010; D. Milisavljevic et al. 2015; A. Corsi et al. 2016, 2017), multiple radio detections, discussed in prior work (magenta; A. Y. Q. Ho et al. 2019, 2020a, b; A. Corsi et al. 2023; G. P. Srinivasaragavan et al. 2024), and with PTF11qcj (A. Corsi et al. 2014), an example of a radio-loud CSM-interacting SN Ic-BL (yellow).

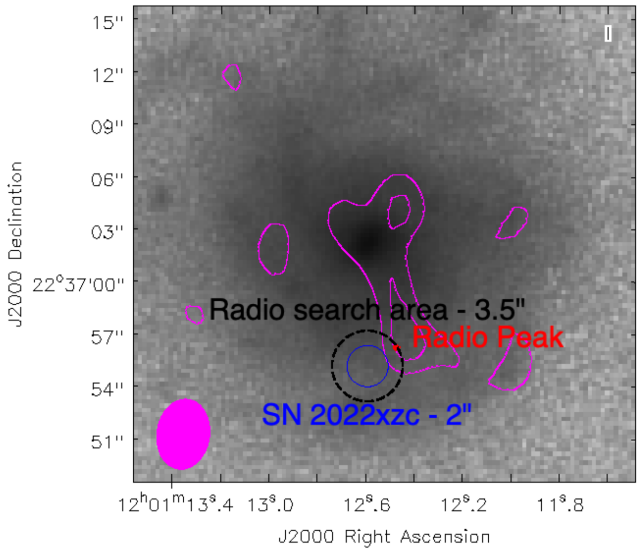

Figure 8. Optical (Pan-STARRS1) image of SN 2022xzc with radio contours mapped in magenta. The radio contours correspond to the first VLA epoch, taken ≈33 days after the estimated explosion time (at 5.5 GHz with the VLA in its C configuration). The black circle marks the optical SN position and has a radius equal to the nominal VLA synthesized beam FWHM for that epoch (3.″5). The blue circle has a radius of 2″, comparable to the positional accuracy of ZTF. The magenta contour lines show that the majority of the radio emission is centered around the host galaxy rather than close to the optical SN position. The location of the peak (red dot) of the radio excess we measure in our search area (black circle) shows that this emission is likely due to contamination from the host galaxy (see Section 3.5.1 for further discussion).

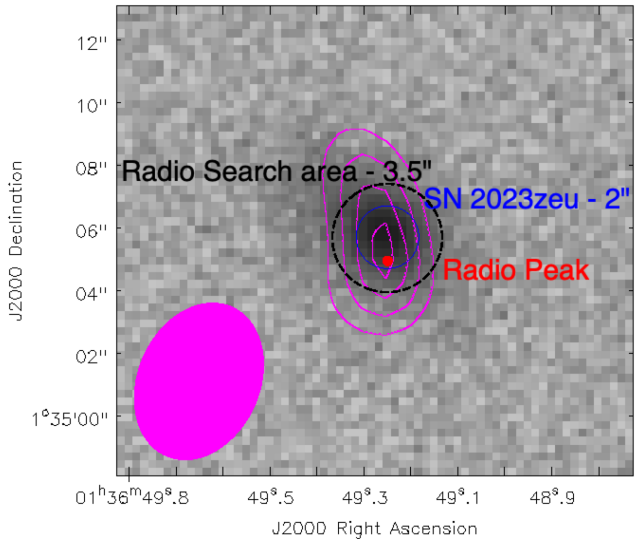

Figure 9. Optical (Pan-STARRS1) image of SN 2023zeu with radio contours mapped in magenta. The radio contours correspond to the second epoch, taken ≈552 days after the estimated explosion time (at 5.5 GHz with the VLA in its C configuration). The black circle marks the optical SN position and has a radius equal to the nominal VLA synthesized beam FWHM for that epoch (3.″5). The blue circle has a radius of 2″, comparable to the positional accuracy of ZTF. The magenta contour lines show that the majority of the radio emission, including the peak (red dot) of the excess radio emission we measure in our VLA search area (black circle), likely originates from the central region of the host galaxy (see Section 3.5.1 for further discussion).

days postexplosion (see Figure 7). SN 2020jqm, analyzed in both A. Corsi et al. (2023) and G. P. Srinivasaragavan et al. (2024), exhibits a double-peaked radio light curve, with the second, stronger peak appearing more than 200 days after the estimated explosion time. A similar source, SN 2021bmf, discussed in G. P. Srinivasaragavan et al. (2024) and S. Anand et al. (2024), displays late-time radio emission emerging after

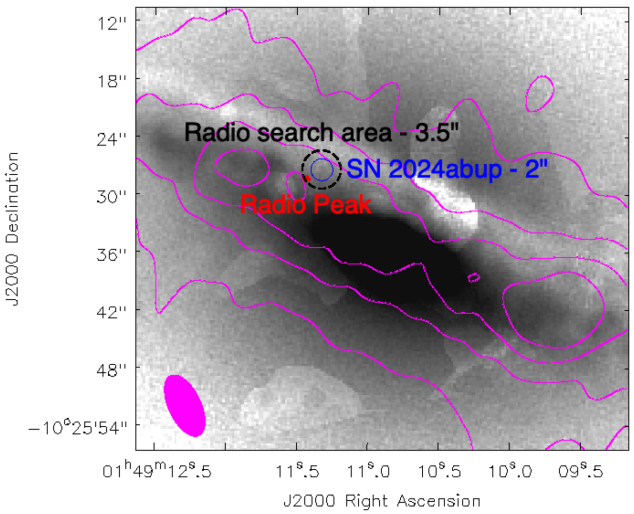

Figure 10. Optical (Pan-STARRS1) image of SN 2024abup with radio contours mapped in magenta. The radio contours correspond to the third epoch, taken ≈195 days after the estimated explosion time (at 5.5 GHz with the VLA in its C configuration). The black circle marks the optical SN position and has a radius equal to the nominal VLA synthesized beam FWHM for that epoch (3.″5). The blue circle has a radius of 2″, comparable to the positional accuracy of ZTF. The magenta contour lines show that the majority of the radio emission, including the peak (red dot) of the excess radio emission we measure in our VLA search area (black circle), likely originates from the central region of the host galaxy (see Section 3.5.1 for further discussion).

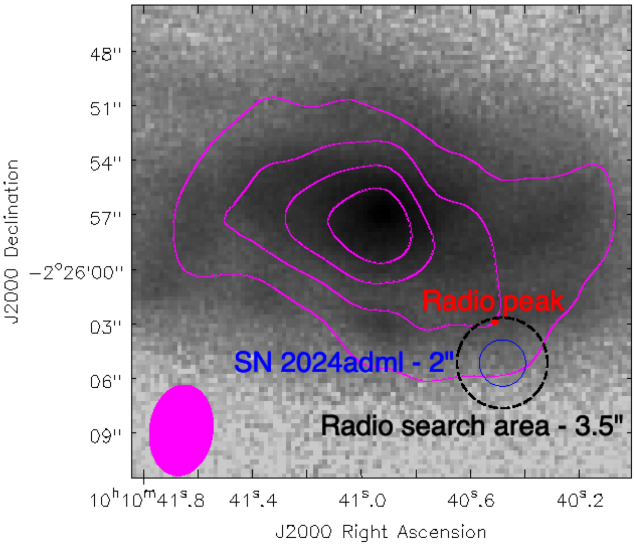

Figure 11. Optical (Pan-STARRS1) image of SN 2024adml with radio contours mapped in magenta. The radio contours correspond to the third epoch, taken ≈181 days after the estimated explosion time (at 5.5 GHz with the VLA in its C configuration). The black circle marks the optical SN position and has a radius equal to the nominal VLA synthesized beam FWHM for that epoch (3.″5). The blue circle has a radius of 2″, comparable to the positional accuracy of ZTF. The magenta contour lines show that the majority of the radio emission, including the peak (red dot) of the excess radio emission we measure in our VLA search area (black circle), likely originates from the central region of the host galaxy (see Section 3.5.1 for further discussion).

∼200 days and peaking after 1000 days postexplosion. Overall, it is clear from Figure 12 that these radio-loud and late-time peaking events show low ejecta speeds and higher progenitor mass-loss rates, suggesting that strong CSM interaction contributes substantially to their radio emission.

Figure 12 also shows that, in addition to the late-time-peaking radio-loud events mentioned above, a second class of radio-emitting SNe Ic-BL is beginning to emerge: Namely, SNe Ic-BL with radio luminosities at least an order of magnitude dimmer than SN 1998bw and smoothly decaying light curves (SN 2018gep, SN 2018bvw, SN 2020bvc, SN 2021ywf, and SN 2022xxf; see Figure 7). These events suggest fastest ejecta speeds of 0.2–0.5c and mass-loss rates $\lesssim 10^{-5}\,M_{\odot}\,\mathrm{yr}^{-1}$.

In what follows, we explore whether these two classes of radio-emitting SNe Ic-BL, neither of which resembles the GRB-associated SN 1998bw, can be interpreted within off-axis and/or lower-energy top-hat jet models (i.e., jet models not already excluded via our X-ray observations), or within models characterized by quasi-spherical ejecta with velocity stratification, possibly accelerated through interaction with choked jets.

In Figure 13, we compare our data with these two model families. While largely off-axis or lower-energy top-hat jets (right panel) may contribute to the late-time emission of some of the radio-loud and late-time peaking SNe (left panel), it is clear that these models generally predict a postpeak radio light-curve decay faster than observed in our data. In contrast, cocoon models with ejecta masses in the range 5×10^{-6}–$10^{-5}\,M_{\odot}$ are broadly compatible with some of the radio-emitting SNe in our sample. More specifically, cocoon models with ejecta masses $1-5 \times 10^{-5}\,M_{\odot}$, a constant-density medium $n = 0.005-0.015\,\mathrm{cm}^{-3}$, microphysical parameters $\epsilon_e = 0.33$ and $\epsilon_B = 0.33$, and maximum ejecta speeds of $\approx 0.74-0.8c$ may explain or contribute to the late-time emission observed in SN 2024rjw and SN 2020jqm. Long-term radio monitoring is critical to distinguish a potential top-hat off-axis jet contribution from a cocoon origin in these events, given that cocoon emission is expected to decay more slowly at very late times. For more information on late-time SNe Ic-BL behavior, we refer the reader to G. Schroeder et al. (2025).

Interestingly, as highlighted in Figure 14, a cocoon model with ejecta mass $2 \times 10^{-6}\,M_{\odot}$, an ISM-like density $n = 1\,\mathrm{cm}^{-3}$, microphysical parameters $\epsilon_e = 0.1$ and $\epsilon_B = 0.01$, and a maximum ejecta velocity of $\approx 0.8c$ provides a good match to the collected radio data of SN 2022xxf. This model is also consistent with the X-ray upper limits. The cocoon contribution to the optical light curve of SN 2022xxf is negligible and therefore does not conflict with the idea that the double-peaked optical light curve of SN 2022xxf is powered by a combination of regular ^{56}Ni decay (powering the first optical hump) and ejecta–CSM interaction (powering the second optical peak; H. Kuncarayakti et al. 2023). In this scenario, the radio emission we observe suggests the presence of a mildly relativistic ejecta tail or cocoon, formed through interaction between the SN shock and the CSM. Late-time radio monitoring (≈1000 days postexplosion) could constrain the presence of potential radio rebrightenings due to interaction with higher-density CSM shells and help distinguish a simple cocoon origin powering the radio emission from a more complex CSM interaction model with shells of varying density (N. T. Palliyaguru et al. 2019).

4. Multimessenger Detection Prospects

SNe associated with cocoons from choked jets have been proposed as promising sources of HE neutrinos. While

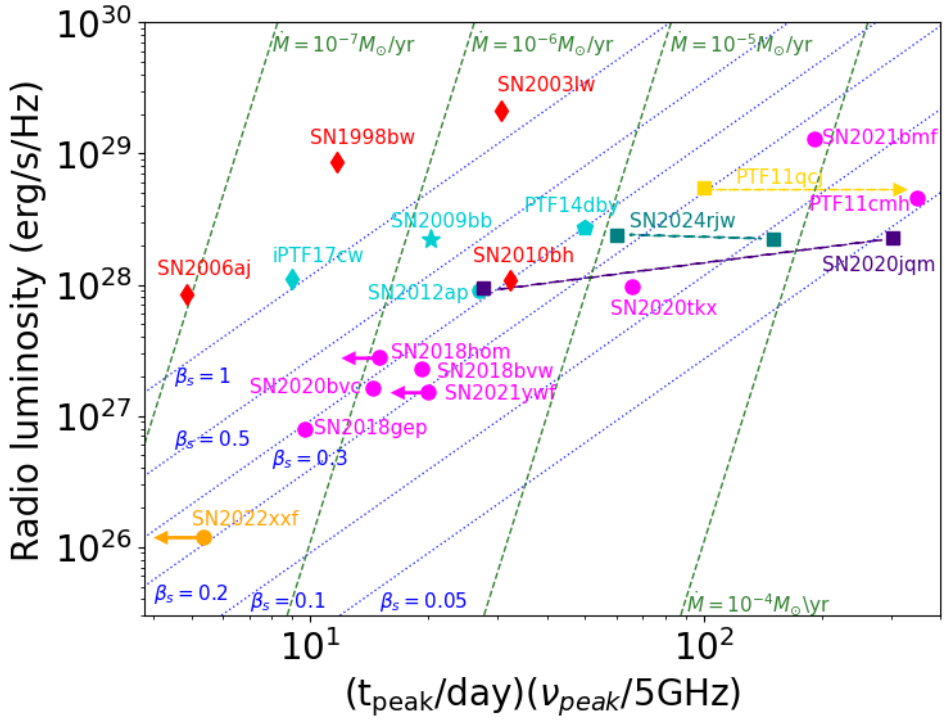

Figure 12. Properties of the radio-emitting ejecta of the SNe in our sample for which we detect a radio counterpart (orange dot) and those detected in previous studies (magenta dots; A. Corsi et al. 2014, 2016, 2017, 2023; G. P. Srinivasaragavan et al. 2024), compared with those of GRB SNe (red diamonds; S. R. Kulkarni et al. 1998; A. M. Soderberg et al. 2004; S. Campana et al. 2006; R. Margutti et al. 2013) and of relativistic-to-mildly relativistic SNe Ic-BL discovered independently of a gamma-ray trigger (cyan; A. M. Soderberg et al. 2010; A. Corsi et al. 2017; D. Milisavljevic et al. 2015). Radio detections with solid arrows indicate lower-limit constraints on the ejecta speeds (β_s normalized to c). SN 2020jqm has a double-peaked radio light curve, and we estimate the radio ejecta speed associated with each of these two peaks. We note that the second radio peak places SN 2020jqm in the region of the parameter space occupied by radio-loud CSM-interacting SNe, similar to PTF11qcj (A. Corsi et al. 2014). SN 2024rjw is a SN Ic with radio emission that supports the interpretation of this event as CSM-interacting, based on the double-peaked optical light curve; see Section 3.5.2 for further discussion.

Table 5
Properties of the Radio-emitting Ejecta for the SNe in Our Sample with Detected Radio Counterparts

SN	β_s	$\dot{M}$ ($M_\odot$ yr^{-1})	E_r (erg)	E_r/E_k
2022xxf	$\gtrsim$0.2	$\lesssim 3 \times 10^{-7}$	$\lesssim 10^{46}$	<0.001%
2024rjw	$\gtrsim$0.2	$\lesssim 10^{-5}$	$\lesssim 6 \times 10^{48}$	<0.2%
	(0.09)	(7×10^{-5})	(5×10^{48})	

Note. From left to right, we report the SN name, the estimated ejecta speed normalized to c (β_s), the progenitor mass-loss rate ($\dot{M}$), the energy coupled to the fastest (radio-emitting) ejecta (E_r), and the ratio between E_r and the total explosion kinetic energy E_k (from optical modeling; see Section 3.5). For SN 2024rjw, we list results for the two brightest detections at $t = 53$ and $t = 133$ days; see Table 4 for details.

successful jets power classical long GRBs, mildly relativistic or failed jets can remain hidden from gamma-ray observatories due to optical thickness or insufficient breakout, but still accelerate hadrons that produce neutrinos via photohadronic interactions. These neutrinos, being weakly interacting, can escape dense stellar envelopes and serve as unique messengers of jet activity inside exploding massive stars (N. Senno et al. 2016).

Several searches using IceCube data have investigated possible neutrino emission from core-collapse SNe, especially those of Type Ib/c (N. Senno et al. 2016, 2018; A. Esmaili & K. Murase 2018; R. Abbasi et al. 2023; P.-W. Chang et al. 2024). However, due to the limited number of detected SNe Ic-BL at the time, none of these studies present dedicated analyses focusing solely on SNe Ic-BL.

We estimate the sensitivity of IceCube to the 15 SNe Ic-BL with radio ejecta speeds β_s between 0.2 and 0.8c and mass-loss rates $\dot{M} \lesssim 10^{-5}\ M_\odot\ \mathrm{yr}^{-1}$ (see Figure 12) via a stacking likelihood analysis based on P.-W. Chang et al. (2024) and B. Zhou et al. (2021), using these SNe and mock IceCube data. The mock IceCube data are based on IceCube public data (R. Abbasi et al. 2021), spanning 2008–2018, over a different time period to our SN sample, allowing us to treat them as background-only (time-independent) in the vicinity of each SN's sky position.

Figure 15 shows the estimated HE neutrino sensitivity (magenta line) of IceCube to the 15 SNe Ic-BL in this work, along with upper limits from a previous analysis of 386 SNe Ib/c (cyan line; P.-W. Chang et al. 2024) at 95% confidence level, compared with IceCube's diffuse astrophysical neutrino flux measurement (blue; M. G. Aartsen et al. 2020). We note that a recent measurement obtained a very similar result (R. Abbasi et al. 2024). Importantly, the sensitivity derived from the 15 SNe Ic-BL is more than twice as strong as the upper limit obtained from the 386 SNe Ib/c sample (P.-W. Chang et al. 2024), and approaches IceCube's measurement (M. G. Aartsen et al. 2020). This is because the 15 SNe Ic-BL are, on average, significantly closer to us, and their small number reduces the cumulative foreground, resulting in a higher signal-to-noise ratio compared to the 386

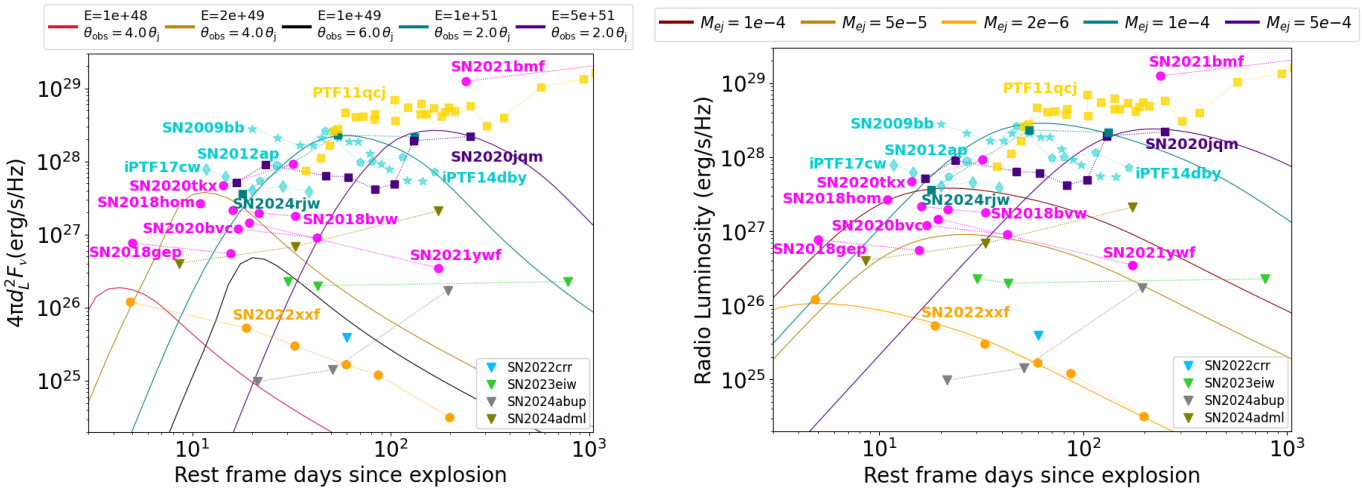

Figure 13. Left: off-axis GRB afterglow model light curves computed with `afterglowpy` (G. Ryan et al. 2020), similar to Figure 6 but with lower energies E and larger off-axis angles (see legend). Overall, these models show postpeak decay that is faster than typically observed in the radio. Right: `afterglowpy` cocoon models (solid lines) with input parameters $\beta_s = 0.71-0.79$, $n = 1$ cm^{-3}(uniform medium), and ejecta masses $M_{\rm ej} = 10^{-5}\,M_\odot - 2\times10^{-6}\,M_\odot$. For SN 2022xxf, a cocoon model with the following parameters $\beta_s = 0.79$, $M_{\rm ej} = 2\times10^{-6}\,M_\odot$ provides an excellent fit; see Section 3.6 for further discussion. We also show cocoon models compatible with SN 2024rjw that may explain the late-time rebrightening of SN 2020jqm. However, we caution that an interpretation of these two SNe within the cocoon model requires extended late-time radio follow-up.

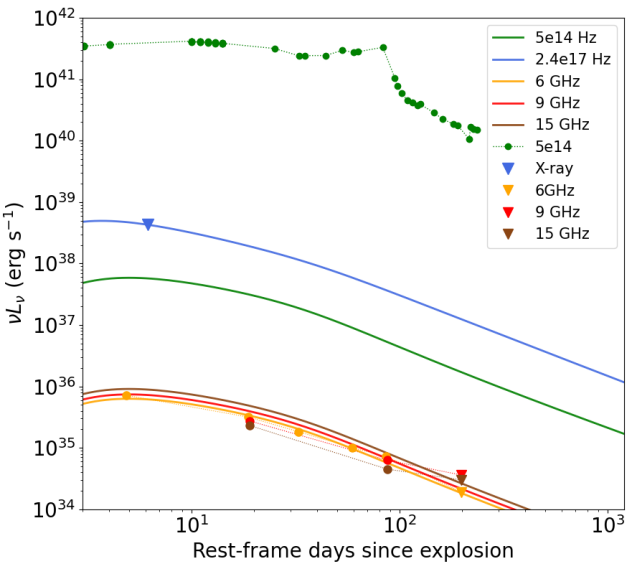

Figure 14. SN 2022xxf observations are compared with predictions from a cocoon model with ejecta mass $2\times10^{-6}\,M_\odot$, an ISM-like density $n = 1$ cm^{-3} (uniform medium), microphysical parameters $\epsilon_e = 0.1$ and $\epsilon_B = 0.01$, and maximum and minimum ejecta velocities of $\approx0.8c$ and $\approx0.1c$, respectively. This model provides a good match to the radio data for SN 2022xxf and agrees with the X-ray upper limits (blue). The contribution of the cocoon model (green solid line) to the optical light curve of SN 2022xxf (green dots and dotted line) is negligible, and hence does not conflict with the idea that the double-peaked optical light curve of SN 2022xxf is powered by a combination of regular ^{56}Ni decay (powering the first optical hump) and ejecta–CSM interaction (powering the second optical peak; H. Kuncarayakti et al. 2023); see Section 3.6 for further discussion.

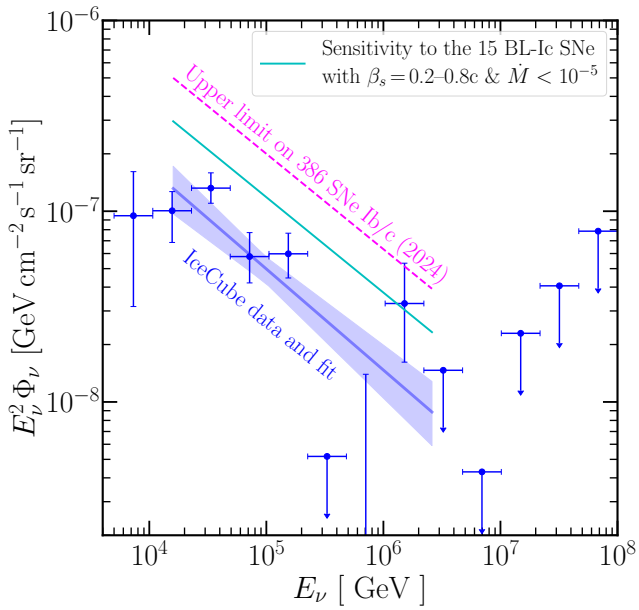

Figure 15. Our estimated HE neutrino sensitivity of an IceCube-like detector to the 15 SNe Ic-BL with radio ejecta speeds β_s between 0.2 and $0.8c$ and mass-loss rates $\dot{M} \lesssim 10^{-5}\,M_\odot$ yr^{-1} (see Figure 12), along with upper limits from a previous analysis of 386 SNe Ib/c from 2008 to 2018 (P.-W. Chang et al. 2024) at 95% confidence level, compared with the diffuse neutrino flux measured by IceCube (M. G. Aartsen et al. 2020). For illustration purposes, the sensitivity and upper-limit lines assume $f_{\rm jet} = 1$, meaning all SNe are assumed to host choked jets aligned toward Earth; see text for details.

SNe Ib/c. Our results indicate that these 15 SNe Ic-BL offer excellent discovery potential if targeted in a dedicated search for HE neutrino emission using IceCube data. We note that the sensitivity and upper-limit lines in Figure 15 assume $f_{\rm jet} = 1$, meaning all SNe are assumed to host choked jets aligned toward Earth. In practice, for a representative Ic-BL sample selected independently of radio emission properties, we expect $f_{\rm jet} < 10\%$, which would scale the sensitivity curves upward by a factor of $\gtrsim$10. This highlights the importance of large samples as well as radio monitoring to identify events most likely associated with cocoons based on their radio properties.

5. Summary and Outlook

We presented radio and X-ray follow-up observations of eight SNe Ic-BL and one SN Ic (SN 2024rjw) from the ZTF sample. Our results confirm that 1998bw-like SNe are

intrinsically rare, and favor the idea that SNe Ic-BL constitute a diverse population of stellar explosions, powered by a range of central engines and circumstellar environments. The continued discovery of mildly relativistic SNe with radio luminosities between $\sim 10^{25}$ and $\sim 3 \times 10^{28}$ erg s^{-1} Hz^{-1} supports the interpretation that radio-emitting stripped-envelope SNe, consistent with off-axis jets or cocoon emission from choked jets, may be relatively common. We demonstrated that at least one out of our sample of nine SNe is fully compatible with a cocoon light-curve model. Across our campaigns, we identify only one event (SN 2022xxf) that falls into the parameter space of SN 2006aj-like explosions, characterized by faint, early-time radio emission peaking just days after explosion. This detection suggests that more SNe Ic-BL may harbor GRB 060218 (SN 2006aj)-like emission but are missed due to the scarcity of early-time radio follow-up. As also highlighted by A. Corsi et al. (2023), rapid spectroscopy and deep radio observations within $\lesssim$5 days of explosion are essential to capture these elusive events.

In the future, the Legacy Survey of Space and Time, conducted by the Vera C. Rubin Observatory (Ž. Ivezić et al. 2019), is poised to revolutionize transient discovery. The upcoming Data Preview 2 in 2026 May will provide a reprocessing of all commissioning data, and once fully operational, Rubin is expected to discover ~1,000,000 SNe per year (M. L. Graham et al. 2024). With a sample of this size, we expect systematic VLA follow-up to provide key evidence for a SN 1998bw-like candidate, or to call into question the currently accepted event rate of low-luminosity GRBs (Section 3.5.3). Fast and accurate spectroscopic classification will be critical to fully exploit this discovery potential by enabling radio and X-ray follow-up. Rubin's data, combined with coordinated radio campaigns, will offer unparalleled opportunities to investigate jet formation, CSM structure, and the diverse end-of-life scenarios for massive stars.

Acknowledgments

T.O-D. and A.C. acknowledge partial support from the NASA Swift guest investigator programs (Cycles 18, 19, 20) via award Nos. 80NSSC23K0314/80NSSC24K1272, 80NSSC24K1273, and 80NSSC25K7623, and from the National Science Foundation (NSF) via award No. AST-2431072. The National Radio Astronomy Observatory and Green Bank Observatory are facilities of the U.S. National Science Foundation operated under cooperative agreement by Associated Universities, Inc. SEDM: SED Machine is based upon work supported by the National Science Foundation under grant No. 1106171. S.A. is supported by an LSST-DA Catalyst Fellowship (grant No. 62192 from the John Templeton Foundation to LSST-DA). S.Y. acknowledges the funding from National Natural Science Foundation of China (grant No. 12303046), the Startup Research Fund of Henan Academy of Sciences (grant No. 242041217), and the Joint Fund of Henan Province Science and Technology R&D Program (grant No. 235200810057). S.A. also gratefully acknowledges support from Stanford University, the United States Department of Energy, and a generous grant from Fred Kavli and The Kavli Foundation. B.Z. is supported by Fermi Forward Discovery Group, LLC under Contract No. 89243024CSC000002 with the U.S. Department of Energy, Office of Science, Office of High Energy Physics. This work is based on observations obtained with the Samuel Oschin Telescope 48-inch and the 60 inch Telescope at the Palomar Observatory as part of the Zwicky Transient Facility (ZTF) project. ZTF is supported by the National Science Foundation under grants Nos. AST-1440341, AST-2034437, and currently Award No. 2407588. ZTF receives additional funding from the ZTF partnership. Current members include Caltech, USA; Caltech/IPAC, USA; University of Maryland, USA; University of California, Berkeley, USA; University of Wisconsin at Milwaukee, USA; Cornell University, USA; Drexel University, USA; University of North Carolina at Chapel Hill, USA; Institute of Science and Technology, Austria; National Central University, Taiwan; and OKC, University of Stockholm, Sweden. Operations are conducted by Caltech's Optical Observatory (COO), Caltech/IPAC, and the University of Washington at Seattle, USA.

Appendix A
SN 2020jqm (ZTF20aazkjfv)

We refer the reader to A. Corsi et al. (2023) and G. P. Srinivasaragavan et al. (2024) for details about this SN Ic-BL. Its P48 light curve and the spectrum used for classification are shown in Figures 1 and 2, respectively.

Appendix B
SN 2021ywf (ZTF21acbnfos)

We refer the reader to A. Corsi et al. (2023), S. Anand et al. (2024), and G. P. Srinivasaragavan et al. (2024) for details about this SN Ic-BL. Its P48 light curve and the spectrum used for classification are shown in Figures 1 and 2, respectively.

Appendix C
SN 2022xzc (ZTF22abnpsou)

Our first ZTF photometry of SN 2022xzc was obtained on 2022 October 17 (MJD 59869.53) with P48. The first detection was in the r band, with a host-subtracted magnitude of 19.17 ± 0.16 mag, at $\alpha = 12^{\rm h}01^{\rm m}12\overset{\rm s}{.}58$, $\delta = +22°36'55''.3$ (J2000). The object was first reported to the TNS by ZTF (2022) on October 18, and first detected by ZTF (2022) on October 17 at $r = 18.17$ mag (C. Fremling 2022). The last ZTF nondetection was on 2022 October 17 at $r > 18.4$ mag. The transient was classified as an SN Type Ic-BL by K. Das et al. (2022) based on spectra taken with ALFOSC on NOT, shown in Figure 2. It has a measured redshift of $z = 0.027$ and is located near the edge of its host galaxy.

Appendix D
SN 2022crr (ZTF22aabgazg)

Our first ZTF photometry of SN 2022crr was obtained on 2022 February 18 (MJD 59628.50) with P48. The first detection was in the g band, with a host-subtracted magnitude of 17.76 ± 0.09mag, at $\alpha = 15^{\rm h}24^{\rm m}49\overset{\rm s}{.}132$, $\delta = -21°23'21''.73$ (J2000). The object was first reported to the TNS by ATLAS (2022) on February 18, and first detected by ATLAS (2022) on February 18 with orange-ATLAS = 17.97 mag (J. Tonry et al. 2022). The last ZTF nondetection was on 2022 April 8 at $g > 19.69$ mag, and the last ATLAS nondetection was on 2022 February 17 at $o > 18.55$ AB mag. The transient was classified as an SN Type Ic-BL by K. Davis et al. (2022) based on spectra taken from the LRIS on the Keck I Telescope in

Hawaii, shown in Figure 2, and found near its host galaxy with a measured redshift of $z = 0.0188$. We also note this source was used in two recent papers, Keck Infrared Spectra Data Release 1 (S. Tinyanont et al. 2024), and the velocity evolution of broad-lined Ic in G. Finneran et al. (2025).

Appendix E
SN 2022xxf (ZTF22abnvurz)

SN 2022xxf is a well-studied transient with double-peaked optical light curves, which can be seen in Figure 1. For detailed information about the spectra and progenitor models of this source, we refer the reader to H. Kuncarayakti et al. (2023). We used spectra obtained with DBSP on the Palomar 200-inch Hale Telescope, shown in Figure 2.

Appendix F
SN 2023eiw (ZTF19aawhzsh)

Our first ZTF photometry of SN 2023eiw was obtained on 2023 March 29 (MJD 60032.15) with P48. The first detection was in the g band, with a host-subtracted magnitude of 18.92 ± 0.10 mag, at $\alpha = 12^{\rm h}28^{\rm m}46\overset{\rm s}{.}200$, $\delta = +46°31'15''.64$ (J2000). The object was first reported to the TNS by Pan-STARRS (2023) on March 31, and first detected by Pan-STARRS (2023) on March 30 at $i = 18.53$ mag by K. C. Chambers et al. (2023). The last ZTF nondetection was on 2023 March 26 at $g > 20.66$ mag. The transient was classified as an SN Type Ic-BL by J. Sollerman et al. (2023) based on spectra taken by SEDM attached to P60. Figure 2 shows spectra taken from ALFOSC on NOT. The supernova host galaxy has a known redshift of $z = 0.025$, measured from SDSS spectroscopy.

Appendix G
SN 2023zeu (ZTF18abqtnbk)

Our first ZTF photometry of SN 2023zeu (ZTF18abqtnbk) was obtained on 2023 December 9 (MJD 60287.11) with P48. The first detection was in the r band, with a host-subtracted magnitude of 18.82 ± 0.10 mag, at $\alpha = 01^{\rm h}36^{\rm m}49\overset{\rm s}{.}249$, $\delta = +01°35'05''.68$ (J2000). The object was first reported to the TNS by ZTF (2023) on December 9, and first detected by ZTF (2023) on December 9 at $r = 18.82$ mag (C. Fremling 2023). The last ZTF nondetection was on 2023 November 20 at $g > 19.21$ mag. The transient was classified as an SN Type Ic-BL by D. Desai (2023) based on spectra taken by the SuperNova Integral Field Spectrograph (SNIFS) on the University of Hawaii 88-inch (UH88) telescope, shown in Figure 2, SN 2023zeu is located within an AGN with a host-galaxy measured redshift of $z = 0.03$.

Appendix H
SN 2024rjw (ZTF24aayimjt)

Our first ZTF photometry of SN 2024rjw (ZTF24aayimjt) was obtained on 2024 August 3 (MJD 60525.30) with P48. The first detection was in the r band, with a host-subtracted magnitude of 20.15 ± 0.20 mag, at $\alpha = 21^{\rm h}03^{\rm m}10^{\rm s}.107$, $\delta = +20°45'02''.58$ (J2000). The object was first reported to the TNS by ZTF (2024a) on August 5, and first detected by ZTF (2024a) on August 3 at $r = 20.15$ mag (J. Sollerman et al. 2024). The last ZTF nondetection was on 2024 July 31 at $g > 20.65$ mag. The transient was classified as an SN Type Ic-BL by C. Angus (2024) based on spectra taken by SNIFS on the UH88 telescope, shown in Figure 2, and has a measured redshift of $z = 0.02$.

Appendix I
SN 2024adml (ZTF24abwsaxu)

Our first ZTF photometry of SN 2024adml (ZTF24abwsaxu) was obtained on 2024 December 12 (MJD 60650.46) with P48. The first detection was in the r band, with a host-subtracted magnitude of 18.36 ± 0.06 mag, at $\alpha = 10^{\rm h}10^{\rm m}40\overset{\rm s}{.}480$, $\delta = -02°26'05''.14$ (J2000). The object was first reported to the TNS by ZTF (2024b) on December 6, and first detected by ZTF (2024b) on December 6 at $r = 18.36$ mag by A. Munoz-Arancibia et al. (2024). The last ZTF nondetection was on 2024 December 4 at $g > 20.10$ mag. The transient was classified as an SN type Ic-BL by J. Duarte et al. (2024) based on spectra taken by the ESO Faint Object Spectrograph and Camera v2 on the New Technology Telescope (3.58m). The spectra taken from ALFOSC on NOT are shown in Figure 2. The SN has a measured redshift of $z = 0.037$.

Appendix J
SN 2024abup (ZTF24abvtbyt)

Our first ZTF photometry of SN 2024abup (ZTF24abvtbyt) was obtained on 2024 December 11 (MJD 60655.17) with P48. The first detection was in the g band, with a host-subtracted magnitude of 16.03 ± 0.06 mag, at $\alpha = 01^{\rm h}49^{\rm m}11\overset{\rm s}{.}320$, $\delta = -10°25'27''.44$ (J2000). The object was first reported to the TNS by ATLAS (2024) on November 22, and first detected by ATLAS (2024) on November 22 with cyan-ATLAS = 17.02 mag by J. Tonry et al. (2024). The last ATLAS nondetection was on 2024 November 21 at $c > 19.48$ mag. The transient was classified initially as a Type Ib/c by C. Balcon (2024), then later as an SN Type Ic-BL by C. Lidman et al. (2024) based on spectra taken by the Wide Field Spectrograph on the Australian National University 2.3 m Telescope. The spectra shown in Figure 2 are taken from the SEDM mounted on P60. The SN has a measured redshift of $z = 0.0058$.

ORCID iDs

Tanner O'Dwyer https://orcid.org/0009-0007-1842-7028
Alessandra Corsi https://orcid.org/0000-0001-8104-3536
Sheng Yang https://orcid.org/0000-0002-2898-6532
Shreya Anand https://orcid.org/0000-0003-3768-7515
S. Bradley Cenko https://orcid.org/0000-0003-1673-970X
Gokul P. Srinivasaragavan https://orcid.org/0000-0002-6428-2700
Anna Y. Q. Ho https://orcid.org/0000-0002-9017-3567
Jesper Sollerman https://orcid.org/0000-0003-1546-6615
Bei Zhou https://orcid.org/0000-0003-1600-8835
Arvind Balasubramanian https://orcid.org/0000-0003-0477-7645
Po-Wen Chang https://orcid.org/0000-0003-1134-0652
Marc Kamionkowski https://orcid.org/0000-0001-7018-2055
Daniel Perley https://orcid.org/0000-0001-8472-1996
Russ R. Laher https://orcid.org/0000-0003-2451-5482
Kohta Murase https://orcid.org/0000-0002-5358-5642
Frank J. Masci https://orcid.org/0000-0002-8532-9395
Mansi M. Kasliwal https://orcid.org/0000-0002-5619-4938

Josiah N. Purdum https://orcid.org/0000-0003-1227-3738
Matthew J. Graham https://orcid.org/0000-0002-3168-0139

References

Aartsen, M. G., Abraham, K., Ackermann, M., et al. 2016, ApJ, 824, 115
Aartsen, M. G., Ackermann, M., Adams, J., et al. 2015, ApJL, 805, L5
Aartsen, M. G., Ackermann, M., Adams, J., et al. 2020, PhRvL, 125, 121104
Abbasi, R., Abdou, Y., Abu-Zayyad, T., et al. 2012, A&A, 539, A60
Abbasi, R., Ackermann, M., Adams, J., et al. 2022, ApJ, 939, 116
Abbasi, R., Ackermann, M., Adams, J., et al. 2023, ApJL, 949, L12
Abbasi, R., Ackermann, M., Adams, J., et al. 2021, arXiv:2101.09836
Abbasi, R., Ackermann, M., Adams, J., et al. 2024, PhRvD, 110, 022001
Anand, S., Barnes, J., Yang, S., et al. 2024, ApJ, 962, 68
Angus, C. 2024, TNSCR, 2024-2929, 1
Arnett, W. D. 1982, ApJ, 253, 785
ATLAS 2022, SN 2022crr, TNS, https://www.wis-TNS.org/object/2022crr
ATLAS 2024, SN 2024abup, TNS, https://www.wis-TNS.org/object/2024abup
Balcon, C. 2024, TNSCR, 2024-4655, 1
Barthelmy, S. D., Barbier, L. M., Cummings, J. R., et al. 2005, SSRv, 120, 143
Bellm, E. C., Kulkarni, S. R., Graham, M. J., et al. 2019, PASP, 131, 018002
Blagorodnova, N., Neill, J. D., Walters, R., et al. 2018, PASP, 130, 035003
Burrows, D. N., Hill, J. E., Nousek, J. A., et al. 2005, SSRv, 120, 165
Campana, S., Mangano, V., Blustin, A. J., et al. 2006, Natur, 442, 1008
Cano, Z. 2013, MNRAS, 434, 1098
Cano, Z., Wang, S.-Q., Dai, Z.-G., & Wu, X.-F. 2017, AdAst, 2017, 8929054
Cardelli, J. A., Clayton, G. C., & Mathis, J. S. 1989, ApJ, 345, 245
Cenko, S. B., Fox, D. B., Moon, D.-S., et al. 2006, PASP, 118, 1396
Chambers, K. C., de Boer, T., Bulger, J., et al. 2023, TNSTR, 2023-689, 1
Chambers, K. C., Magnier, E. A., Metcalfe, N., et al. 2016, arXiv:1612.05560
Chang, P.-W., Zhou, B., Murase, K., & Kamionkowski, M. 2024, PhRvD, 109, 103041
Chevalier, R. A. 1992, ApJ, 394, 599
Chevalier, R. A. 1998, ApJ, 499, 810
Corsi, A., Cenko, S. B., Kasliwal, M. M., et al. 2017, ApJ, 847, 54
Corsi, A., Eddins, A., Lazio, T. J. W., Murphy, E. J., & Osten, R. A. 2024, FrASS, 11, 1401792
Corsi, A., Gal-Yam, A., Kulkarni, S. R., et al. 2016, ApJ, 830, 42
Corsi, A., Ho, A. Y. Q., Cenko, S. B., et al. 2023, ApJ, 953, 179
Corsi, A., Ofek, E. O., Gal-Yam, A., et al. 2014, ApJ, 782, 42
Coughlin, M. W., Bloom, J. S., Nir, G., et al. 2023, ApJS, 267, 31
Das, K., Meynardie, W., Chu, M., & Fremling, C. 2022, TNSCR, 2022-3317, 1
Davis, K., Foley, R., & Dimitriadis, G. 2022, TNSCR, 2022-520, 1
De Colle, F., Kumar, P., & Aguilera-Dena, D. R. 2018, ApJ, 863, 32
De Colle, F., Kumar, P., & Hoeflich, P. 2022, MNRAS, 512, 3627
Dekany, R., Smith, R. M., Riddle, R., et al. 2020, PASP, 132, 038001
Desai, D. 2023, TNSCR, 2023-3201, 1
Djupvik, A. A., & Andersen, J. 2010, ASSP, 14, 211
Duarte, J., Santos, R., Milligan, A., et al. 2024, TNSCR, 2024-4837, 1
Eisenberg, M., Gottlieb, O., & Nakar, E. 2022, MNRAS, 517, 582
Esmaili, A., & Murase, K. 2018, JCAP, 2018, 008
Evans, P. A., Beardmore, A. P., Page, K. L., et al. 2009, MNRAS, 397, 1177
Finneran, G., Cotter, L., & Martin-Carrillo, A. 2025, A&A, 700, A200
Fremling, C. 2022, TNSTR, 2022-3035, 1
Fremling, C. 2023, TNSTR, 2023-3177, 1
Fremling, C., Miller, A. A., Sharma, Y., et al. 2020, ApJ, 895, 32
Gehrels, N., Chincarini, G., Giommi, P., et al. 2004, ApJ, 611, 1005
Graham, M. L., Bellm, E., Guy, L., et al. 2024, LSST Alerts: Key Numbers DMTN-102, Vera C. Rubin Observatory https://dmtn-102.lsst.io/
Graham, M. J., Kulkarni, S. R., Bellm, E. C., et al. 2019, PASP, 131, 078001
Granot, J., De Colle, F., Ramirez-Ruiz, E., et al. 2018, MNRAS, 481, 2711
Hernáandez, A. C. V., & Andernach, H. 2018, arXiv:1808.07178
Ho, A. Y. Q., Corsi, A., Cenko, S. B., et al. 2020b, ApJ, 893, 132
Ho, A. Y. Q., Goldstein, D. A., Schulze, S., et al. 2019, ApJ, 887, 169
Ho, A. Y. Q., Kulkarni, S. R., Perley, D. A., et al. 2020a, ApJ, 902, 86
Ivezić, Ž., Kahn, S. M., Tyson, J. A., et al. 2019, ApJ, 873, 111
Iwamoto, K., Mazzali, P. A., Nomoto, K., et al. 1998, Natur, 395, 672
Kim, Y.-L., Rigault, M., Neill, J. D., et al. 2022, PASP, 134, 024505
Kulkarni, S. R., Frail, D. A., Wieringa, M. H., et al. 1998, Natur, 395, 663
Kuncarayakti, H., Sollerman, J., Izzo, L., et al. 2023, A&A, 678, A209
Law, C. J., Gaensler, B. M., Metzger, B. D., Ofek, E. O., & Sironi, L. 2018, ApJL, 866, L22
Lazzati, D., Morsony, B. J., Blackwell, C. H., & Begelman, M. C. 2012, ApJ, 750, 68
Li, W., Leaman, J., Chornock, R., et al. 2011, MNRAS, 412, 1441
Li, Z.-Y., & Chevalier, R. A. 1999, ApJ, 526, 716
Liang, E., Zhang, B., Virgili, F., & Dai, Z. G. 2007, ApJ, 662, 1111
Lidman, C., Rauf, L., Auchettl, K., et al. 2024, TNSCR, 2024-4668, 1
Liu, Y.-Q., Modjaz, M., Bianco, F. B., & Graur, O. 2016, ApJ, 827, 90
Lyman, J. D., Bersier, D., & James, P. A. 2014, MNRAS, 437, 3848
Lyman, J. D., Bersier, D., James, P. A., et al. 2016, MNRAS, 457, 328
Margutti, R., Soderberg, A. M., Wieringa, M. H., et al. 2013, ApJ, 778, 18
Masci, F. J., Laher, R. R., Rusholme, B., et al. 2019, PASP, 131, 018003
Mazzali, P. A., Deng, J., Maeda, K., et al. 2002, ApJL, 572, L61
Mazzali, P. A., Deng, J., Nomoto, K., et al. 2006b, Natur, 442, 1018
Mazzali, P. A., Deng, J., Pian, E., et al. 2006a, ApJ, 645, 1323
Mazzali, P. A., Deng, J., Tominaga, N., et al. 2003, ApJL, 599, L95
Mazzali, P. A., Iwamoto, K., & Nomoto, K. 2000, ApJ, 545, 407
McMullin, J. P., Waters, B., Schiebel, D., Young, W., & Golap, K. 2007, ASPC, 376, 127
Meegan, C., Lichti, G., Bhat, P. N., et al. 2009, ApJ, 702, 791
Milisavljevic, D., Margutti, R., Parrent, J. T., et al. 2015, ApJ, 799, 51
Modjaz, M., Li, W., Butler, N., et al. 2009, ApJ, 702, 226
Modjaz, M., Liu, Y. Q., Bianco, F. B., & Graur, O. 2016, ApJ, 832, 108
Munoz-Arancibia, A., Bauer, F. E., Pignata, G., et al. 2024, TNSTR, 2024-4779, 1
Murphy, E. J., Condon, J. J., Schinnerer, E., et al. 2011, ApJ, 737, 67
Muthukrishna, D., Parkinson, D., & Tucker, B. E. 2019, ApJ, 885, 85
Nakar, E. 2015, ApJ, 807, 172
Nakar, E., & Piran, T. 2017, ApJ, 834, 28
Nakar, E., & Sari, R. 2012, ApJ, 747, 88
Oke, J. B., Cohen, J. G., Carr, M., et al. 1995, PASP, 107, 375
Oke, J. B., & Gunn, J. E. 1982, PASP, 94, 586
Pais, M., Piran, T., & Nakar, E. 2023, MNRAS, 519, 1941
Palliyaguru, N. T., Corsi, A., Frail, D. A., et al. 2019, ApJ, 872, 201
Pan-STARRS 2023, SN 2023eiw, TNS, https://www.wis-TNS.org/object/2023eiw
Patat, F., Cappellaro, E., Danziger, J., et al. 2001, ApJ, 555, 900
Perley, D. A., Fremling, C., Sollerman, J., et al. 2020, ApJ, 904, 35
Perley, R. A., Chandler, C. J., Butler, B. J., & Wrobel, J. M. 2011, ApJL, 739, L1
Pian, E., Mazzali, P. A., Masetti, N., et al. 2006, Natur, 442, 1011
Rigault, M., Neill, J. D., Blagorodnova, N., et al. 2019, A&A, 627, A115
Rodríguez, Ó., Maoz, D., & Nakar, E. 2023, ApJ, 955, 71
Ryan, G., van Eerten, H., Piro, L., & Troja, E. 2020, ApJ, 896, 166
Sauer, D. N., Mazzali, P. A., Deng, J., et al. 2006, MNRAS, 369, 1939
Schlafly, E. F., & Finkbeiner, D. P. 2011, ApJ, 737, 103
Schroeder, G., Ho, A. Y. Q., Dastidar, R. G., et al. 2025, ApJ, 995, 61
Senno, N., Murase, K., & Mészáros, P. 2016, PhRvD, 93, 083003
Senno, N., Murase, K., & Mészáros, P. 2018, JCAP, 2018, 025
Sharma, Y., Sollerman, J., Meynardie, W., et al. 2025, PASP, 137, 094101
Shivvers, I., Modjaz, M., Zheng, W., et al. 2017, PASP, 129, 054201
Soderberg, A. M., Chakraborti, S., Pignata, G., et al. 2010, Natur, 463, 513
Soderberg, A. M., Chevalier, R. A., Kulkarni, S. R., & Frail, D. A. 2006a, ApJ, 651, 1005
Soderberg, A. M., Kulkarni, S. R., Berger, E., et al. 2004, Natur, 430, 648
Soderberg, A. M., Kulkarni, S. R., Berger, E., et al. 2005, ApJ, 621, 908
Soderberg, A. M., Nakar, E., Berger, E., & Kulkarni, S. R. 2006b, ApJ, 638, 930
Sollerman, J., Meynardie, W., & Chu, M. 2023, TNSCR, 2023-778, 1
Sollerman, J., Fremling, C., Perley, D., & du Laz, T. 2024, TNSTR, 2024-2774, 1
Srinivasaragavan, G. P., Yang, S., Anand, S., et al. 2024, ApJ, 976, 71
Sun, H., Zhang, B., & Li, Z. 2015, ApJ, 812, 33
Taddia, F., Sollerman, J., Fremling, C., et al. 2019, A&A, 621, A71
Tinyanont, S., Foley, R. J., Taggart, K., et al. 2024, PASP, 136, 014201
Tonry, J., Denneau, L., Weiland, H., et al. 2022, TNSTR, 2022-436, 1
Tonry, J., Denneau, L., Weiland, H., et al. 2024, TNSTR, 2024-4579, 1
Tonry, J. L., Denneau, L., Heinze, A. N., et al. 2018, PASP, 130, 064505
van der Walt, S. J., Crellin-Quick, A., & Bloom, J. S. 2019, JOSS, 4, 1247
Wellons, S., Soderberg, A. M., & Chevalier, R. A. 2012, ApJ, 752, 17

Willingale, R., Starling, R. L. C., Beardmore, A. P., Tanvir, N. R., & O'Brien, P. T. 2013, MNRAS, 431, 394
Yang, S., & Sollerman, J. 2023, ApJS, 269, 40
Yaron, O., & Gal-Yam, A. 2012, PASP, 124, 668
Zegarelli, A., Guetta, D., Celli, S., et al. 2024, A&A, 690, A187
Zhao, X.-H., & Cheng, K.-F. 2022, Univ, 8, 588
Zhou, B., Kamionkowski, M., & Liang, Y.-f. 2021, PhRvD, 103, 123018
ZTF 2022, SN 2022xzc, TNS, https://www.wis-TNS.org/object/2022xzc
ZTF 2023, SN 2023zeu, TNS, https://www.wis-TNS.org/object/2023zeu
ZTF 2024a, SN 2024rjw, TNS, https://www.wis-TNS.org/object/2024rjw
ZTF 2024b, AT 2024adm, TNS, https://www.wis-TNS.org/object/2024adm